This is a preprint, the final version is subject to change, of the American Mineralogist (MSA)
Cite as Authors (Year) Title. American Mineralogist, in press.
DOI: https://doi.org/10.2138/am-2019-6980

Revision 1

Epidote spherulites and radial euhedral epidote aggregates in a metavolcanic breccia in the Dabie UHP metamorphic belt (China): implication for dynamic metamorphism

An-Ping Chen[1, 2], Jian-Jun Yang[1, 2, *], Da-Lai Zhong[1, 2], Yong-Hong Shi[3] and Jing-Bo Liu[1, 2]

[1]State Key Laboratory of Lithospheric Evolution, Institute of Geology and Geophysics, Chinese Academy of Sciences, Beitucheng Xilu 19, P.O. Box 9825, Beijing 100029, China

[2]University of Chinese Academy of Sciences, Beijing 100049, China

[3]School of Resources and Environment Engineering, Hefei University of Technology, Tunxi Lu 193, Hefei 230009, China

[*]Corresponding author: jjyang@mail.igcas.ac.cn

Running title: Epidote spherulites and radial euhedral epidote aggregates

This is a preprint, the final version is subject to change, of the American Mineralogist (MSA)
Cite as Authors (Year) Title. American Mineralogist, in press.
DOI: https://doi.org/10.2138/am-2019-6980

ABSTRACT

Epidote spherulites are identified in a greenschist facies metavolcanic breccia enclosing a body of coesite-bearing eclogite at Ganghe in the Dabie ultrahigh-pressure metamorphic belt, east-central China. The epidote spherulites are formed by fibrous, radially arranged, and rare earth element (REE)-rich epidote crystals (REE = 0.13–0.36 (or slightly higher) cations per formula unit, cpfu) and interfibrillar REE-poor epidote (REE ≤0.10 cpfu). Some of the epidote spherulites are overgrown by radially arranged euhedral epidote crystals, which also form aggregates around preexisting quartz, plagioclase, and/or epidote. The epidote grains in such aggregates display oscillatory zoning, with REE content varying from a negligible amount to about 0.44 cpfu. Epidote also occurs as REE-poor individual euhedral crystals about the radial epidote aggregates or form loose clusters of randomly oriented crystals. Thermodynamic modeling of the mineral assemblages in the plagioclase pseudomorphs and in the matrix shows that they formed at greenschist facies metamorphic conditions (435–515 °C and 5–7 kbar). The spherulites and radial euhedral crystal aggregates, however, do not belong to these assemblages and are non-equilibrium textures. They imply crystal growth under large degrees of supersaturation, with relatively low ratios of the diffusion rate (D) to the crystal growth rate (G). At low D/G ratios, spiky interfaces are favourable for diffusion-controlled growth and the resultant texture is a collection of spikes around a growth center, forming a spherulite. The change of epidote texture from spherulite to radial euhedral crystal aggregates implies a decrease of supersaturation and an increase of D/G, such that the crystal morphology was controlled by its crystallographic structure. The crystallization of the individual epidote grains corresponds to a further drop of supersaturation and a further

increase of the *D/G* ratio, approaching to the equilibrium conditions. Transiently higher *P*-*T* conditions are inferred from the spherulite-forming reactions, relative to the *P*-*T* estimates for the equilibrium assemblages. The fibrous crystals in the spherulites having relatively large interfacial energies would inevitably adjust their shapes to equilibrium ones with low interfacial energies if the *P*-*T*-H_2O conditions were maintained for a sufficiently long period of time. The non-equilibrium epidote aggregates likely formed in response to *P*-*T* and fluid pulses, possibly related to seismicity.

Key words: Dabieshan, epidote, non-equilibrium, radial euhedral crystal aggregates, spherulite, supersaturation

INTRODUCTION

Spherulite is a radial aggregate of fibrous crystals (Vernon 2004). It can be formed by silicates, metal alloys, elements, organic molecules and synthetic polymers, crystallized from melts, solids, solutions or gels (Shtukenberg et al. 2011). The driving force of crystallization, which measures the distance from equilibrium, is an important factor in controlling the crystal morphology. It is well known that crystal shape changes from polyhedral, skeletal, dendritic to spherulitic with an increasing driving force (e.g., Lofgren 1974; Oaki and Imai 2003; Jones 2017). Such a relationship is also supported by theoretical modeling (Saito and Ueta 1989; Sunagawa 1999; Wilbur and Ague 2006; Gránásy et al. 2014). It is therefore established that no matter what materials and physical states are involved, the conditions required by the crystallization of spherulites are highly non-equilibrium.

In crystalline rocks, spherulites can be formed by the same or different minerals and are known to crystallize from supercooled volcanic or frictional melts, devitrifying glasses, or supercooled fluids (e.g., Lofgren 1971a, 1971b; Vernon 2004; Xu and Scott 2005; Lin 2008; Watkins et al. 2009; Gardner et al. 2012; Melinger-Cohen et al. 2015; Jones 2017). Spherulitic epidote aggregates have been described in pseudomorphs after plagioclase in altered rhyolites (Hudson 1937), quartz-feldspar porphyry clasts in conglomerates (McCann and Kennedy 1974), high-pressure pseudotachylytes (Austrheim and Andersen 2004; Petley-Ragan et al. 2018), and in schists (Misch, 1965). Van Staal et al. (1990) mentioned epidote spherulites in pseudomorphs after pumpellyite in a blueschist.

Radial epidote aggregates other than spherulitic forms are described in hydrothermally altered rocks (Blattner 1976; Carpenter and Walker 1992; Harper 1995; Torres-Alvarado 2002; Minakawa et al. 2008; Melinger-Cohen et al. 2015; Owens and Dymek 2016), pegmatites or

veins (Ross 1941; Halcrow 1956; Nehlig and Juteau 1988), teschenites (Kitchen 1985) and various types of metamorphic rock (Heinrich 1964; Stout 1964; Misch 1965; Stuart-Smith 1990; Barriga and Fyfe 1997; Brunsmann et al. 2000; Rebay and Messiga 2007; Pascual et al. 2013). The morphology of individual epidote crystals constituting these aggregates is diverse, including acicular, skeletal and prismatic. Misch (1965) described epidote aggregates with crystal shapes varying from radial fibrous through radial tapering to non-radial lumpy in a suit of crossite schists and actinolitic greenschists. Melinger-Cohen et al. (2015) reported both epidote spherulites and radial euhedral epidote aggregates growing in two adjacent zones of amygdules in an epidotized basalt.

Although the epidote spherulites in pseudotachylytes can be readily accepted to be evidence for quenching, in the other reports of epidote spherulites in metamorphic rocks the growth mechanisms and kinetic implications of the texture have been barely discussed. The present study describes a sequence of epidote textures including spherulites, radial euhedral crystal aggregates, and individual euhedral crystals in a metavolcanic breccia enclosing a coesite-bearing eclogite body at Ganghe in Dabieshan, east-central China. The growth mechanisms of these epidote textures and their implication for a possible dynamic and non-equilibrium metamorphic process are discussed. The data presented may form part of a basis for the eventual understanding of the hosting of the Triassic coesite-bearing eclogite by the Neo-Proterozoic greenschist facies metavolcanic breccia.

GEOLOGICAL SETTING AND FIELD OCCURRENCE

The Ganghe locality is in central Dabieshan, known as an ultrahigh-pressure (UHP) metamorphic terrane (Zhang et al. 2009). The main rock types at Ganghe are UHP gneisses, eclogites, metagranitoid, marble, jadeite-quartzite, a suite of low-grade metamorphic rocks

(LGMRs), crosscut by late granitoid and lamprophyre dykes (Schmid et al. 2003; Guo et al. 2012). The LGMRs are considered to be a part of a cover unit that was tectonically juxtaposed against the UHP gneisses of Yangtze basement (Schmid et al. 2003). Zircon dating and Sm-Nd whole-rock analysis of the LGMRs yielded an ^{207}Pb-^{206}Pb age of 745–802 Ma and an isochron age of 790.9 ± 18.6 Ma, respectively (Dong et al. 2002). Zircon in a volcanic breccia yielded an $^{206}Pb/^{238}U$ age of 761 ± 33 Ma (Schmid et al. 2003). Both results are interpreted to be the protolith age. Whole-rock oxygen isotope analysis shows that they have a low $\delta^{18}O$ range of −0.4‰ to 4.6‰, suggesting meteoric-hydrothermal alteration prior to metamorphism (Zhou et al. 2001; Zheng et al. 2003). The protolith ages and oxygen isotope characteristics of the LGMRs are generally comparable with those of UHP metamorphic rocks, with which they together form an integral part of the Dabie orogen (Zheng et al. 2005).

The epidote textures described here are observed in one type of the LGMRs, a greenschist facies metavolcanic breccia. The rock is well exposed with a foliation dipping 25° to 45° toward 105° to 145° in a length of about 40 m near the Ganghe Bridge. It is separated from a nearby granitic gneiss by a shear zone and is intruded by several unmetamorphosed lamprophyre dykes. A thin wedge-shaped coesite-bearing eclogite body (7 m × 50 cm) is enclosed in the metavolcanic breccia (Fig. 1a). The eclogite body shows increasing retrogression outward from fresh eclogite in the core to biotite-epidote-amphibolite and then to a schistose layer (<5 cm) of biotite + epidote + plagioclase + quartz at the contact with the metavolcanic breccia. The foliation in the retrogressed eclogite is in accordance with that of the enclosing metavolcanic breccia.

PETROGRAPHY

The host rock

The metavolcanic breccia contains both crystal and lithic fragments (>60 vol%) immersed in a fine-grained matrix (Fig. 1b). The foliation of the breccia is defined by oriented phengite flakes which wraps around the slightly elongated volcanic fragments. The matrix (grain size generally <100 μm) is composed of quartz, plagioclase, phengite, K-feldspar, epidote, Fe-Ti oxide, with minor biotite, garnet, chlorite, titanite and apatite. The crystal fragments are quartz (1 mm–1 cm), plagioclase (generally >1 mm) and hematite (1–5 mm). The quartz fragments consist of fine-grained (<100–500 μm) polygonal quartz aggregates. Plagioclase fragments are pseudomorphosed by Na-Pl + Ep + Ph ± Kfs ± Qz (mineral abbreviations after Whitney and Evans, 2010). In the plagioclase pseudomorphs some grains of phengite and epidote appear acicular. Skeletal garnet is frequently observed where hematite is present nearby. Some of the plagioclase fragments are partially replaced along their grain boundaries and fractures by a more Na-rich and fine-grained plagioclase or K-feldspar. Hematite fragments are commonly altered to rutile and/or titanite and are surrounded by garnet coronas. Oriented lamellae are frequently observed in hematite fragments.

The lithic fragments are angular to subround with their longest dimension in the range of <5 mm to 8 cm (Fig. 1b). They are subround, irregularly-shaped or elongated, commonly oriented to the foliation. The most common type of lithic fragments is albitophyre, whose porphyritic texture can well be recognized despite the metamorphic alteration. The phenocrysts (plagioclase, quartz and hematite) are replaced as in the case of crystal fragments. The cryptocrystalline matrix of the albitophyre fragment is composed of plagioclase, quartz and hematite, with minor amounts of phengite, K-feldspar, epidote (often with small REE-rich cores), garnet, titanite and apatite. Some lithic fragments consist entirely of fine-grained (<100 μm) minerals and are relatively rich in plagioclase, K-feldspar, Fe-Ti oxide or quartz

compared with the matrix. Some fragments (1 mm–2 cm) rich in fine-grained phengite and epidote are heterogeneously distributed in the matrix (Fig. 1c). Fine-grained aggregates of REE-rich epidote + apatite are occasionally found in the matrix. In places, epidote is observed in fine-grained plagioclase and/or quartz aggregates.

The epidote textures

The description of the epidote textures below is based on photomicrographs (Figs. 2a and 2f) and backscattered electron images from a field emission scanning electron microscope (other images in Fig. 2, and Figs. 1c and 3). Epidote spherulites are observed both in the matrix and in the lithic fragments, which is formed by fine-grained (<100 μm) garnet, phengite, biotite, plagioclase, K-feldspar, epidote, quartz and Fe-Ti oxide. The spherulites are commonly fan-shaped (Figs. 2a, 2b, 2d and 2e), some having irregular shapes (Fig. 2c). Their sizes range from 20 μm × 20 μm to 200 μm × 400 μm. They consist of radiating brighter REE-rich epidote fibers, with the spaces in between filled by darker REE-poor epidote (Figs. 2b–2e). The fibers in the spherulites show extinctions at slightly different angles and in places display sweeping extinctions (Fig. 2a). Some of the spherulites include or emanate from quartz and relatively coarser REE-poor epidote grains (Figs. 2b, 2d, 3b, 3d, S1a and S1b). The width of the epidote fibers is variable from one spherulite to another (e.g., ~5 μm in Fig. 2d and <2 μm in Figs. 2e and S1c) and within a single spherulite, in which they are coarser in the core and become increasingly finer outward (Figs. 2b, 2d and S1b). The fibers branch outward, with new fibers splitting from a parent fiber (Figs. 2e and S1c). In some cases, finer epidote fibers grew nearly perpendicular to the thicker ones, forming a feathery dendrite-like texture (lower part of Fig. 3d, enlarged in Fig. S1d). Relatively coarse grains of epidote, K-feldspar and quartz and fine rounded particles of hematite and zircon are found to be included in the

spherulites (Figs. 2d, 3b, S1b and S2c). Almost all of the radiating points of the observed spherulites are characterized by randomly oriented bits of the bright epidote (REE-richer) being separated by coarser dark (REE-poorer) epidote (Figs. 2b–2d and S1b). In one of the several epidote aggregates at a boundary between a lithic fragment and the matrix, the epidote spherulite cores appear to have broken into small bits, which are cemented by REE-poor epidote (Fig. 3d). The REE-poor epidote are further overgrown by fan-shaped epidote spherulites and dendrites in the outer parts of the texture.

In many cases, the fibers of the epidote spherulites are continued by euhedral epidote laths (2 μm × 5 μm to 20 μm × 100 μm) outwards in the same directions (Figs. 2a–2d, 3b and S1b). Similar to the spherulites, such radial epidote laths are also variable in brightness, reflecting variable REE contents (Figs. 2b–2d, 3b and S1b). Euhedral epidote crystals (10 μm × 40 μm to 50 μm × 120 μm) also form radial aggregates around plagioclase, quartz or epidote (Figs. 1c and 2f–2h), some having minute bright dots in their cores (Fig. 2g). These aggregates occur both in the matrix and in the lithic fragments (Figs. 1c, 2g and 2h). Many of the radial epidote aggregates on the border of the fragment are cut off and only parts of them are preserved in the fragment (Fig. 1c). The epidote grains in such a texture commonly display compositional zoning, with alternating bright and dark zones mimicking the euhedral shapes of the crystals (Figs. 2g, 2h and S1b). Fine-grained garnet, phengite and biotite are commonly included in the radial epidote crystals overgrowing the spherulites (Figs. 2c and 3b). Where foliation is conspicuous, it is at large angles to or crosscut by some fibers of the epidote spherulites or the overgrowing radial euhedral epidote laths (Figs. 3a–3d and S2a–S2d). Randomly oriented individual euhedral epidote grains (3 μm × 10 μm to 100 μm × 200 μm) are scattered around the epidote spherulites and the radial epidote aggregates (Figs. 1c, 2d, 2f

187 and 2h), or form loose epidote clusters in the matrix (Fig. S1e).

188 **MINERAL COMPOSITIONS**

189 Epidote compositions were analyzed by using a wavelength-dispersive electron microprobe
190 analyser (JEOL JXA-8100) at the State Key Laboratory for Mineral Deposits Research,
191 Nanjing University. Accelerating voltage and beam current were maintained at 15 kV and 20
192 nA, respectively. The electron beam diameter was 1 μm. As the accelerated electrons were
193 scattered by the sample, the interaction volume between the electron beam and the sample
194 (thus the sample volume analyzed) has an overall dimension somewhat larger than the ideal
195 incident beam diameter. Due to this effect, the fine epidote fibers (<1–3 um) cannot be
196 analyzed precisely but for each analysis only an average of the fiber and the interfibrillar
197 epidote is yielded. Therefore, the chemical formulae of the analyses (e.g., No. 5 in Fig. S1a,
198 No. 6 and No. 7 in Fig. S1c) are only approximations and provide lower values for the REE
199 content. All standards used in the analysis are from the American National Standards Institute
200 (ANSI) except for thorianite, which is from the Université de Toulouse. Amphibole is used for
201 the standards of Si, Ti, Fe, Mg, Ca, Na and K. Topaz and Fe-carpholite are used for the
202 standards of Al and Mn, respectively. REE-1 is used for the standard of Eu and Gd, REE-2 for
203 Sm and Nd, REE-3 for La, Ce, Pr and Y, and thorianite for Th. Detection limits (1σ level) for
204 the elements are: La (0.1%), Ce (0.1%), Pr (0.07%), Nd (0.06%), Sm (0.12%), Eu (0.09%),
205 Gd (0.08%), Y (0.02%) and Th (0.02%). The ZAF method was applied for the matrix
206 corrections. Other minerals were analyzed by an electron microprobe analyzer (JOEL-8100)
207 at the Institute of Geology and Geophysics, Chinese Academy of Sciences. Analytical
208 conditions are the same, except for a larger beam diameter (1–5 μm) used in some cases.
209 Diopside is used for the standard of Si, Mg and Ca, rutile for Ti, hematite for Fe, bustamite
for

Mn, albite for Na, and potassium feldspar for K. Synthetic oxides Al_2O_3 and Cr_2O_3 are used for the standards of Al and Cr, respectively. All standards are from SPI Supplies except for potassium feldspar, which is from P&H Developments Ltd. Detection limits (1σ level) for the elements are: Si (0.01%), Ti (0.015%), Al (0.01%), Cr (0.015%), Fe (0.015%), Mn (0.01%), Ni (0.02%), Mg (0.01%), Ca (0.01%), Na (0.01%) and K (0.01%). Mineral formulae were calculated assuming stoichiometry and charge balance and the Fe^{3+}/Fe^{2+} ratios were estimated according to Droop (1987).

Epidote

The structural formula of the epidote-group minerals can be expressed by $A_2M_3Si_3O_{12}(OH)$ (Dollase 1971), in which A = Ca, Sr, Pb^{2+}, Mn^{2+}, Th, REE^{3+} and U, and M = Al, Fe^{3+}, Fe^{2+}, Mn^{3+}, Mn^{2+}, Mg, Cr^{3+} and V^{3+} (Deer et al, 1986). The main cations in the epidote analyzed here are Ca, REE, Mn^{2+}, Al, Fe^{2+}, Fe^{3+}, Mg and Si, among which Ca, Mn^{2+} and REE are assigned to the A sites, and Al, Mg, Fe^{2+} and Fe^{3+} are assigned to the M sites. The substitution of Ca by REE on the A sites is charge balanced by equal amounts of substitution of trivalent cations (Al, Fe^{3+}) by divalent cations (Fe^{2+}, Mg) on the M sites, expressed as the exchange vector REE(Mg, Fe^{2+})Ca_{-1}(Fe^{3+}, Al)$_{-1}$. The sums of the cations on the A sites of several analyses are slightly less than 2 (Table 1), probably caused by the presence of minor amounts of other elements not analyzed (e.g., Sr, Pb and U) on the A sites. The REE-Al diagram shows that the epidote analyses are variable in allanite component (Fig. 4). The term epidote is used here in a broad sense.

The epidote crystals in different textures have variable concentrations of REE, which is dominated by La, Ce, Pr, Nd, Sm, Eu and Gd, with minor amount of Y detected in some cases (Fig. 4; Table 1). The ThO_2 contents in all of the analyses are below detection limit and are

omitted in Table 1. The analyses of the REE-rich fibrous epidote in the spherulites are represented by $(Ca_{1.56–1.82}Na_{0.00–0.01}REE_{0.13–0.36}Mn_{0.03–0.06})(Mg_{0.01–0.05}Fe^{2+}_{0.14–0.36}Fe^{3+}_{0.53–0.71}Al_{2.03–2.25})Si_{2.98–3.02}Ti_{0.00–0.01}O_{12}(OH)$. The relatively wide interfibrillar epidote in the spherulites is lower in REE content ($(Ca_{1.84–1.96}REE_{0.02–0.10}Mn_{0.02–0.06})(Mg_{0.00–0.01}Fe^{2+}_{0.00–0.14}Fe^{3+}_{0.64–0.77}Al_{2.13–2.23})Si_{2.99–3.03}O_{12}(OH)$), accompanied by lower Mg and Fe^{2+} and higher Ca and Fe^{3+} contents (Table 1). The round epidote inclusions in the center of the spherulites are similar in REE contents with the interfibrillar epidote.

The euhedral epidote overgrowing the spherulites is similar in Al content to the interfibrillar epidote but is lower in REE and Fe^{2+} and higher in Ca and Fe^{3+} contents ($(Ca_{1.90–1.99}REE_{0.01–0.05}Mn_{0.01–0.06})(Mg_{0.00–0.01}Fe^{2+}_{0.00–0.05}Fe^{3+}_{0.75–0.85}Al_{2.13–2.25})Si_{2.97–3.02}O_{12}(OH)$, Fig. 4). The darker euhedral epidote in the radial aggregates is poor in REE and shows slight variations in $Fe^{3+}/(Fe^{3+} + Al)$ ratio from 0.25 to 0.28 (Figs. 2h and 4; Table 1). The epidote displaying oscillatory zoning in the radial euhedral crystal aggregates is variable in REE content ($(Ca_{1.38–1.90}Na_{0.00–0.02}REE_{0.01–0.44}Mn_{0.03–0.11})(Mg_{0.00–0.07}Fe^{2+}_{0.00–0.34}Fe^{3+}_{0.43–0.75}Al_{2.06–2.27})Si_{3.00–3.02}Ti_{0.00–0.01}O_{12}(OH)$), from negligible in the dark zones to about 0.44 cations per formula unit in some of the bright zones (Figs. 2g and 4; Table 1). The randomly oriented individual euhedral epidote grains have the similar range in $Fe^{3+}/(Fe^{3+} + Al)$ ratio with the REE-poor epidote grains in the radial euhedral epidote (Table 1).

Other minerals

Garnet is variable but generally high in spessartine (15–50 mol%) and low in pyrope (2–8 mol%), with variable proportions of grossular and almandine ($Prp_{2–8}Alm_{31–59}Grs_{10–45}Sps_{15–50}$, Table 2). Garnet composition is variable in the same texture and its compositional ranges for different textures are overlapped. The dark rims of the plagioclase are albite-rich (Ab = 95–98

mol%) while its interior and the plagioclase in other textures are oligoclase (Ab = 83–92 mol%). K-feldspar is low in anorthite (<1 mol%) and albite (3–7 mol%) contents. The Si content in phengite ranges from 3.14 to 3.28, with a Fe^{2+}/Mg ratio varying from 1.5 to 2.3 (Table 2). Biotite has a Fe^{2+}/Mg ratio from 0.8 to 1.2 and an Al content from 1.30 to 1.42. The coarse hematite fragments ($Hem_{64–85}Ilm_{15–31}Pph_{0.5–3}$) are poorer in pyrophanite content and richer in hematite content compared with the oriented lamellae ($Hem_{0–5}Ilm_{43–52}Pph_{47–53}$) in them. Fine-grained hematite in the matrix is close to end-member composition ($Hem_{80–100}Ilm_{0–20}Pph_{0–3}$).

P-T-H_2O ESTIMATES

The *P-T*-H_2O estimates were carried out by thermodynamic calculations using THERMOCALC (Powell et al. 1998) and an internally consistent thermodynamic dataset (Holland and Powell 2011). The thermodynamic models of relevant minerals are as follows: garnet (White et al. 2007), clinopyroxene (Green et al. 2007), amphibole (Diener et al. 2007), epidote (Holland and Powell 1998), feldspars (Holland and Powell 2003), biotite (White et al. 2007), and muscovite (Coggon and Holland 2002). Quartz, kyanite and lawsonite are taken to be pure phases. Two approaches are used to constrain the *P-T*-H_2O conditions of the equilibrium assemblages. The first one is thermobarometry for the matrix assemblage of the metavolcanic breccia (Pl + Ph + Kfs + Ep + Bt + Grt + Hem + Sph + Qz, mineral compositions in Table 2). To avoid the problem of uncertainty in fluid composition, the equilibria used involve only the solid phases. Only a set of linearly independent equilibria is selected for the thermobarometry, according to their dependence on pressure and temperature. The intersections of the selected equilibria yield *P-T* estimates of 5.5–6 kbar and 475–485 °C (Fig. 5a). The oxygen fugacity for this matrix assemblage was estimated through the

intersections of the O_2-bearing equilibria in a T-$\log_{10}(fO_2)$ diagram (P = 6 kbar), which yield the $\log_{10}(fO_2)$ ranging from −22.7 to −22.4 (Fig. 5b).

Another approach used is phase diagram modeling of the plagioclase pseudomorphs, which appear to contain equilibrium assemblages (Pl + Ph + Ep ± Kfs ± Qz). Garnet is not considered for this assemblage because it is closely associated with hematite inclusions in the plagioclase pseudomorphs. To take into account the compositions of all the minerals constituting the plagioclase pseudomorphs, the model system was chosen to be Na_2O-CaO-K_2O-FeO-MgO-Al_2O_3-SiO_2-H_2O-Fe_2O_3 (NCKFMASHO). The bulk composition used by THERMOCALC is estimated by using the relationship for each oxide:

$$M\left(\mathrm{R_mO_n}\right)=\sum_{i=1}^{k}\left(p_i\left(\sum_{j=1}^{l}x_{ij}C_j\left(\mathrm{R_mO_n}\right)\right)\right)$$

where $M(\mathrm{R_mO_n})$ is the molar percentage of the oxide $\mathrm{R_mO_n}$ in the bulk composition, p_i is the molar percentage of mineral i in the rock sample, x_{ij} is the mole fraction of the end-member j in the mineral i calculated using the mineral composition data (Table 3), $C_j(\mathrm{R_mO_n})$ is the stoichiometric coefficient of the oxide $\mathrm{R_mO_n}$ in the end-member j, k is the number of minerals considered and l is the number of end-members in the mineral i. The p_i is calculated by:

$$p_i=\left(v_i/V_i\right)/\sum_{i=1}^{k}\left(v_i/V_i\right)$$

where v_i is the volume percentage of mineral i in the rock sample, V_i is the molar volume of i and is estimated by:

$$V_i=\sum_{j=1}^{l}\left(x_{ij}V_{ij}\right)$$

where V_{ij} is the molar volume of the end-member j in the mineral i. The standard state molar volumes of the mineral end-members from Holland and Powell (2011) are used to

approximate V_{ij}, which are in reality not constants but are functions of P and T. For each mineral, v_i is approximated by the area proportions occupied by the mineral on the backscattered electron (BSE) images of the plagioclase pseudomorphs. This method for estimating bulk composition is essentially the same as that of Lanari and Engi (2017) and Centrella et al (2018), who use weight percentages instead of molar percentages.

The average area proportions of the minerals in the plagioclase pseudomorphs are: Pl = 75.7%, Kfs = 10.6%, Ph = 8.7%, Ep = 3.8% and Qz = 1.2%. With these data and the relationships given above the bulk composition is estimated to be (in mol%): SiO_2=70.20, Al_2O_3=14.78, CaO=3.03, MgO=0.31, FeO=0.98, K_2O=2.03, Na_2O=8.40, and Fe_2O_3=0.22. The phase diagram calculated using this bulk composition contains biotite in addition to the observed minerals in the plagioclase pseudomorphs. Also, the calculated plagioclase composition is somewhat richer in albite component compared with the observed plagioclase composition. To reproduce the observed assemblage and plagioclase composition, the bulk composition was slightly adjusted by adding Al_2O_3 and CaO and subtracting SiO_2, FeO and Na_2O (by less than 10% for each oxide). The final bulk composition then becomes (in mol%): SiO_2=69.74, Al_2O_3=15.77, CaO=3.27, MgO=0.33, FeO=0.91, K_2O=2.17, Na_2O=7.60, and Fe_2O_3=0.21. Such an adjustment may be warranted in view of the several factors that affect the accuracy of the estimated composition. For example, the use of area proportions to approximate volume proportions can cause up to 17% error in the estimated bulk composition, and the limited numbers of BSE images used for image processing can also be a source of significant error in the estimation (Lanari and Engi, 2017).

A *P*-*T* diagram with quartz, phengite and H_2O in excess shows that the observed assemblages (Pl + Ph + Ep ± Kfs ± Qz) in the plagioclase pseudomorphs are stable in a large

P-T range of 400 °C to 650 °C and 4 kbar to 14 kbar (Fig. 5c). K-feldspar has a wide stability range in the diagram due to the fact that K_2O is much higher than MgO and FeO and only a small part of K_2O is combined with MgO and FeO to form phengite and biotite, with the rest amount of K_2O forming K-feldspar. To investigate the H_2O condition required by the stability of the assemblage, a *P-M*(H_2O) diagram (Fig. 5d) was calculated at 450 °C. The *P-M*(H_2O) diagram shows that the observed assemblages are confined to four adjacent regions by H_2O-saturation and Kfs and Omp/Jd-absent lines (Fig. 5d). The assemblage Pl + Ph + Ep + Kfs + Qz is restricted within a very narrow region at about 5 kbar above and below the H_2O-saturation line. The assemblage Pl + Ph + Ep + Qz is stable in the *M*(H_2O) range of 4.4–5.0 mol% (corresponding to 1.21–1.38 wt%) H_2O.

To better constrain the *P-T* conditions for the formation of the plagioclase pseudomorphs, mineral composition isopleths are contoured in the field of the H_2O-saturated assemblage (Pl + Ph + Ep + Qz + H_2O, Fig. 5c). The isopleth value of anorthite in plagioclase (X_{An}) increases with both temperature and pressure. The isopleth value of Si in phengite changes in a similar way to anorthite, while the isopleth of paragonite in phengite (X_{Pg}) is nearly parallel to the pressure axis. The stability of the assemblage is more sensitive to pressure than temperature. Therefore, the isopleths of anorthite in plagioclase and paragonite in phengite are chosen to make the *P-T* estimation. The majority of the plagioclase and phengite analyses are in the X_{An} range of 0.08–0.10 and the X_{Pg} range of 0.034–0.040 (Table 3), corresponding to a *P-T* range of 5–7 kbar and 435–515 °C (shaded quadrilateral, Fig. 5c). A few plagioclase analyses have X_{An} above 0.12 and/or X_{Pg} below 0.03, which are plotted outside of the stability field of the assemblage. The *P-T* estimates by thermobarometry and phase diagram modeling are broadly consistent, both pointing to greenschist facies metamorphism.

DISCUSSION

Possible origin of the radial epidote aggregates

Natural spherulites are thus far mostly found in igneous and sedimentary rocks. They are considered to have crystallized from supercooling/supersaturated melts, glasses or solutions. Spherulites are also described or mentioned in some metamorphic rocks, although their origin and petrological significance has barely been addressed. For the radial epidote aggregates (spherulites and radial euhedral epidote aggregates) in the metavolcanic breccia studied here, four different origins are considered. These include: crystallization from (a) volcanic melts or glasses or post-volcanic hydrothermal fluids; (b) shock-induced amorphous materials; (c) solute-rich metamorphic fluid; (d) fluid-mediated metamorphic reactions.

Crystallization from volcanic melts or glasses or post-volcanic hydrothermal fluids. Volcanic spherulites generally have compositions similar to those of their bulk rocks. For example, the spherulites crystallized from supercooling rhyolitic melts are generally composed of SiO_2 polymorphs, sodic plagioclase and alkali feldspar (e.g., Castro et al. 2008; Watkins et al. 2009; Befus et al. 2015), those crystallized from supercooling basaltic melts are generally composed of olivine, pyroxene and calcic plagioclase (e.g., Lofgren 1971a; Monecke et al. 2004; Soule et al. 2006). The fact that the composition of the epidote spherulites is incompatible to the felsic bulk composition of the host volcanic breccia indicates that the epidote spherulites did not crystallize from the volcanic melt or glass.

Melinger-Cohen et al. (2015) describe epidote spherulites and radial euhedral epidote aggregates forming two distinct zones in amygdules in a basalt from northern Michigan and suggest that they crystallized from a hydrothermal fluid during cooling of the rock. Spherulites crystallized from post-volcanic hydrothermal fluid forming amygdules are close

(see below for definition of close and open spherulites), round in shape, and have sharp smooth boundaries. In contrast, the spherulites reported in the present study are more open (wider interfibrillar areas), variable in shape, and have irregular boundaries. The crystallization of spherulites filling vesicles starts from the walls of the pore spaces, whereas in the present case the REE-rich epidote fibers emanate from the centers of the spherulites.

Almost all the epidote spherulites reported here are fragmented and cemented by REE-poor epidote (Figs. 2b–2d, 3b, 3d and S1b). However, the radially overgrowing epidote laths and euhedral crystals are not fragmented except for those on border of the lithic fragments (Fig. 1c). In some cases, metamorphic minerals (phengite, garnet, biotite, and hematite) are included in the overgrowing zones. The inclusion minerals are all found as coarser grains in the surrounding matrix (Figs. 2b–2d, 3b and S1b). Some epidote fibers and overgrowing radial epidote laths are oriented at large angles to or crosscut the foliation (Figs. 3a–3d and S2a–S2d). In Fig. 3b, for example, the foliation formed by oriented phengite, biotite and hematite grains does not affect the shapes of the epidote fibers and laths but instead are stopped or indented by the epidote laths. These observations indicate that brittle deformation occurred after the formation of the epidote spherulites, but before the radiating overgrowth of the epidote laths and euhedral crystals.

The radial euhedral epidote aggregates occur both in the fragments and in the matrix of the breccia (Fig. 1c). Those on the border of a fragment are cut off and only parts of them are left (Fig. 1c), suggesting that they formed both before and after brecciation. Therefore, the brecciation was more likely tectonic and occurred during greenschist facies metamorphism, long after the volcanic brecciation. Some of the radial euhedral epidote aggregates contain bright bits of REE-rich epidote in their cores, suggesting growth on fragmented spherulites.

Epidote in such a texture in places includes biotite and hematite and indent phengite and biotite (Figs. 2g and 2h), indicating that they grew over the metamorphic mica.

To conclude, the radial euhedral epidote aggregates, in places overgrowing the epidote spherulites, are certainly of metamorphic origin. The epidote spherulites are likely also metamorphic. Similar epidote textures were described elsewhere in low grade metamorphic rocks (Misch, 1965; Van Staal et al. 1990).

Crystallization from shock-induced amorphous materials. Analogous to the devitrification of supercooling volcanic glasses, it is possible to form spherulites from glasses of other origins. Non-equilibrium textures formed by metamorphic microlites (e.g., spherulitic, dendritic, skeletal, acicular and poikilitic crystals) in variably eclogitized granulites and gabbros are suggested to have formed in seismic events (Austrheim and Boundy 1994; Austrheim and Anderson 2004; John and Schenk 2006; Yang et al. 2014a, 2014b, 2017; Putnis et al. 2017). In the metavolcanic breccia studied here, the epidote spherulites, the fine grains of metamorphic minerals in the plagioclase pseudomorphs, and the skeletal garnet may be considered to be microlites. The volcaniclastic fabric is preserved although the igneous minerals are replaced by metamorphic minerals. This is in accordance with shock metamorphism, in which the original fabric of the protolith is generally preserved (Feldman 1994; Yang et al. 2017). Epidote spherulites of similar size to the ones studied here are observed in eclogite facies pseudotachylytes (Austrheim & Andersen, 2004; Petley-Ragan et al., 2018). It is possible, therefore, that the epidote spherulites in the metavolcanic breccia crystallized from amorphous materials produced by a seismic event (Su et al. 2006; Nakamura et al. 2015; Yang et al. 2017). The materials needed for the crystallization of epidote may be from the igneous Ca-rich plagioclase and Fe-bearing minerals, such as biotite and hematite, in

addition to fluid.

Crystallization from a solute-rich metamorphic fluid. The local presence of epidote in the anhydrous quartz and feldspar aggregates in the Ganghe metavolcanic breccia may suggest that they crystallized directly from an infiltrating metamorphic solute-rich hot fluid phase. However, the fact that no apparent fluid conduit is observed around the epidote spherulites does not imply a large scaled fluid infiltration. These epidote spherulites are also unrelated to open fluid-filled pores or cavities, suggesting that the fluid migration was rather local and at a very small scale, possibly along grain boundaries. The sporadic occurrence of the radial epidote aggregates also implies that their crystallization was unrelated to widespread fluid ingress. Based on mineral proportions and their H_2O contents, the H_2O content in the phengite dominated fragment containing several radial epidote aggregates (80 vol% Ph + 9 vol% Ep + 10 vol% Pl + 1 vol% Grt) is estimated to be about 3.7 wt% (Fig. 1c). The H_2O content in the plagioclase pseudomorphs ranges from 0.2 wt% to 1.7 wt%, with the proportions of phengite and epidote varying from about 35 vol% and 5 vol% to about 3 vol% and 2 vol%, respectively. The nearly anhydrous aggregates dominated by K-feldspar, plagioclase, and quartz contain very small proportions of hydrous minerals (epidote <5 vol% and phengite <5 vol%) and <0.4 wt% of H_2O. The variable degrees of H_2O-saturation in different textural domains are inconsistent with large scaled H_2O saturated regional metamorphism. The sharp boundaries and the lack of prevailing reaction products between the fragments and the matrix suggest that pervasively fluid-rich conditions were not attained and the transport distances of materials were small, for otherwise the boundaries between the fragments and the matrix would have been obliterated (Etheridge et al. 1983; Walther and Wood 1984). However, if the crystallization was in a very brief metamorphic event (see

discussion below), it may be envisioned that some small domains or grain boundaries in the rock may be transiently H_2O-rich, such that H_2O-saturated assemblages were produced locally (Fig. 5d) (Rubie 1986).

The REE-rich epidote + apatite ± thorite assemblages are interpreted to be the breakdown product of igneous monazite during metamorphism (Finger et al. 1998). The REE-rich epidote + apatite aggregates are occasionally found in the matrix of the metavolcanic breccia at Ganghe. Therefore, the REE for the formation of the epidote spherulites may have derived internally in the rock, via the breakdown of the REE-bearing igneous minerals such as monazite and plagioclase. However, the possibility that the REE were introduced by the fluids cannot be excluded. A quantitative evaluation of gains or losses of the REE during the fluid-rock interactions requires mass balance calculations by using the whole-rock REE contents of variably altered rocks (Ague, 2017; Centrella et al. 2016). This approach, however, is not attempted in the present case because the differently altered samples of the metavolcanic breccia needed for the calculations are not identified in the field.

Crystallization from fluid-mediated metamorphic reactions. The highly non-equilibrium nature of spherulites may have formed through significantly overstepped metamorphic reactions. Reaction overstepping may be related to delayed nucleation due to sluggish crystallization kinetics caused by slow diffusion rate, deficiency of fluid, or absence of deformation (Ridley and Thompson 1986; Wilbur and Ague 2006; Austrheim 2013). Overstepped reactions may be triggered by infiltration of fluid that facilitates the component diffusion. In such a case, the crystallization conditions can be highly non-equilibrium and the compositional gradients around the growing crystal are large. The reaction rate can be fast due to a large free energy change (Rubie 1998). Such a mechanism was proposed to interpret the

radial texture of fibrous or dendritic garnet cores overgrown by euhedral garnet rims in some greenschist facies to amphibolite facies metamorphic rocks (Wilbur and Ague 2006). The overstepping of garnet-forming reactions was suggested to be caused by hindered garnet nucleation, related to the refractory nature of reactant spinel and product garnet. In the case of Ganghe, the growth of the radial epidote crystals around preexisting minerals indicates delayed nucleation. The overstepping of a reaction can be due to deviations of *P*, *T* or composition from the equilibrium state (Pattison et al. 2011). A *P*-*T*-fluid pulse, for example, may cause a hydration reaction to take place in a non-equilibrium manner (see below).

As is discussed below, for any of the above mentioned origins for the formation of the epidote spherulites to be realistic, it is necessary to involve a transient change of *P*, *T*, and/or fluid conditions resulting in overstepping of the REE-rich epidote-forming reactions and restoring back quickly to the original conditions, such that the highly non-equilibrium epidote textures could have formed and preserved.

Kinetics of epidote crystallization in the different textures

The epidote spherulites. Lofgren (1974) defined spherulites with interfibrillar areas filled by visible melt and foreign material to be open spherulites and those with tightly interwoven fibers to be closed. He also distinguished coarse and fine spherulites by a fiber thickness of 3–5 μm. The epidote spherulites described here consist of REE-rich epidote fibers of <3–5 μm and visible interfibrillar REE-poor epidote (Figs. 2b–2e). They are thus considered to be open and fine spherulites.

Considering thermodynamics, a large driving force (Gibbs free energy change) is necessary for the crystallization of spherulites (e.g., Sunagawa 1999; Oaki and Imai 2003; Jones 2017). From kinetics point of view, the ratio of the diffusion rate (*D*) to the crystal

484 growth rate (G) is a controlling factor of the crystal shape (Lofgren 1980; Kirkpatrick 1981).
485 The spherulitic crystal form is favourably developed at small D/G values (Keith and Padden
486 1963; Lofgren 1974; Donaldson 1976; Corrigan 1982; Baker and Freda 2001). When the
487 diffusion rate is much slower than the growth rate, the components rejected by the growing
488 crystal (impurities) are concentrated around the interface while the components required by
489 the growing crystal (nutrients) are depleted around the interface. Volumes away from the
490 growing crystal interface featured by more nutrients and less impurities are the only possible
491 places for further crystal growth and spiky interfaces are favourable for continuous growth
492 (Keith and Padden 1963; Lofgren 1971a). Thus the resultant crystal shape is a collection of
493 spikes around a growth center, forming spherulitic or dendritic shapes.
494 The temperature dependence of REE partitioning behavior of the epidote-group minerals
495 suggests that the REE-rich epidote crystallizes at a higher temperature than the REE-poor
496 epidote (Frei et al. 2003). During the spherulite formation, LREE, Mg and Fe^{2+} were
497 preferentially incorporated into the epidote fibers leaving Al and Fe^{3+} for the later formation
498 of the interfibrillar epidote. This compositional variation implies that the REE-rich epidote
499 fibers and REE-poor interfibrillar epidote crystallized successively in a cooling process.
500 The growth of the epidote spherulites in the metavolcanic breccia at Ganghe likely occurred
501 at a low D/G value under a high degree of supersaturation, far from equilibrium. The
502 epidote-forming reaction may be written involving the observed minerals in the textures and
503 surrounding areas as:
504 $$Pl + Kfs + Bt + Qz + Fluid \rightarrow Ep + Ph + Grt \quad (1)$$
505 From this it can be inferred that the reaction occurred via dissolution of the reactants and
506 precipitation of the products, and that the rate-controlling step was likely the diffusion rate of

Al in the fluid. The growth rate (G) and D/G ratio are estimated by using the relationship (Walther and Wood 1984; Rubie 1986):

$$G = -\frac{2VDC\delta\tau\Delta G_r}{RTdx} \quad (2)$$

where V is the molar volume of epidote and ΔG_r is the Gibbs free energy change for the epidote-forming reaction (cf. Fig. 6a) calculated using the thermodynamic dataset of Holland and Powell (2011) and the activities of the mineral end-members and a reduced H_2O activity (assumed to be 0.5), which is needed in order that the reaction is intersected by the P-T path; d is the final average grain diameter of the epidote spherulites (here taken to be 100 μm), x is the radius of the growing epidote spherulites. The crystal nucleus radius at the initial time of crystallization assumed to be 1 nm (Rubie 1986). R is the gas constant and T is the initial crystallization temperature in K. Following Walther and Wood (1984), it is assumed that the grain boundary diffusion coefficient of Al (D) under H_2O-saturated conditions is 10^{-16} $m^2 \cdot s^{-1}$; the concentration of Al (C) is 3.0×10^4 $mol \cdot m^{-3}$, the thickness of the grain boundary (δ) is 100 nm, and the constant accounting for the non-linear path of the component (τ) is 0.7.

In this scenario, the estimated P-T conditions (Figs. 5a–5c) for the matrix assemblage represent the ambient P-T rather than the P-T spike for the crystallization of the epidote spherulites. Quantitative P-T estimates for the spherulites are difficult to make. In view of the presence of Na-plagioclase and absence of omphacite in the rock, a pressure increase to the average pressure between reaction (3) and the reaction Jd + Qz = Ab (about 11 kbar) and an associated slight increase in temperature to 520 ºC are assumed for this P-T evolution of the epidote spherulites (Fig. 6a). Based on the above assumptions the initial growth rate of the epidote spherulites is calculated to be about 2.7×10^{-9} $m \cdot s^{-1}$. The ratio D/G is then 3.8×10^{-8} m,

a very small value as expected for the growth of spherulites. The uncertainties in these estimates mainly come from the uncertainty of diffusion rate. The G varies sympathetically with D by the same order of magnitude. Although the P-T path for the spherulites is poorly constrained (Fig. 6a), the uncertainty arisen from it is much smaller. For example, if the P-T pulse is assumed to have reached lower values of 7 kbar and 490 °C, the initial G and the D/G ratio are estimated to be 3.1×10^{-10} m·s^{-1} and 3.2×10^{-7} m, respectively, also very small values for the preferential growth of spherulites.

The epidote-forming reaction (Fig. 6a) used in the above estimation of growth rate does not involve the REE components in the epidote spherulites, which cannot be taken into account due to the lack of thermodynamic data for the REE-bearing epidote end-members and fluid. This and the assumption of H_2O activity equal to 0.5 add uncertainties in the calculated ΔG_r and growth rate. Given the highly non-equilibrium and diffusion-controlled nature of crystallization, it is assumed that the epidote spherulites began to crystallize when $-\Delta G_r$ exceeded $0.4RT$, below which the crystallization is considered to be very close to equilibrium and the crystal growth is interface-controlled (Walther and Wood 1984; Rubie, 1986). With this lowest $-\Delta G_r$, a conservative initial G and a corresponding high D/G are then estimated to be 2.5×10^{-10} m·s^{-1} and 4.2×10^{-7} m, respectively. These estimates are independent of the positions of the reaction in Fig. 6a and the P-T path. Therefore, the conclusion that the initial growth rate was large and the growth was diffusion-controlled is unchanged despite the large uncertainties involved in the estimation. In view of the fibrous feature of the epidote crystals, the above estimation of growth rate is again conservative because the collection of radiating fibers and interfibrillar crystals is approximated by a solid sphere.

The radial euhedral epidote aggregates. The radial euhedral epidote aggregates growing

552 on the spherulites or preexisting minerals represent a new stage of epidote crystallization
553 (Figs. 2a–2d, 3b and S1b). A similar change of epidote growth texture was described in a
554 basalt (Melinger-Cohen et al. 2015), in which epidote spherulites and radial euhedral crystal
555 aggregates form two separate zones in amygdules. These two zones are interpreted to have
556 formed during two distinct stages of hydrothermal metamorphism corresponding to changes
557 of the degree of supersaturation or supercooling (Melinger-Cohen et al. 2015). Misch (1965)
558 described epidote glomeroblasts in a suit of crossite and actinolitic schists and distinguished
559 three continuous crystallization stages according to epidote texture. The texture changes from
560 radial fibrous crystal aggregates through radially arranged tapering crystals to granoblastic
561 mosaics of lumpy grains. Misch (1965) noted that the number of crystals in a given
562 glomeroblast progressively decreased and the epidote grains evolved toward a single
563 porphyroblast.

564 Such a change of texture was also produced in experimental crystallization of aromatic
565 hydrocarbon melt, in which spherulites formed at a supercooling of 59 °C were overgrown by
566 radial euhedral crystals at a supercooling of 9 °C (Magill and Plazek 1967). Monte Carlo
567 simulations suggest that the change of garnet texture in a metapelite and a metaultramafic
568 rock from dendritic or spherulitic cores to euhedral rims corresponds to decreases in the
569 degree of supersaturation (Wilbur and Ague 2006).

570 The above natural and experimental observations imply that the radial euhedral crystal
571 aggregates should grow at a degree of supersaturation/supercooling that is lower than that
572 required by the growth of spherulites but higher than that of the single euhedral crystals.
573 Therefore, the radial euhedral epidote aggregates is also a texture formed in a process
574 significantly far from equilibrium. The change of crystal size and shape from fine and fibrous

575 to coarse and euhedral corresponds to a significant drop of the supersaturation and an
576 increased *D*/*G* ratio. Such a texture may be explained by assuming that *D* is comparable to *G*,
577 such that the nutrients and the impurities can be more effectively diffused to and away from
578 the growing interface, and the component concentration is essentially homogeneous around
579 the growing crystal. In this case, the crystal morphology is likely controlled by its
580 crystallographic structure and the resultant crystal is euhedral (Vernon 2004). The radiation of
581 the crystals from preexisting minerals implies a low nucleation rate.

582 **The individual euhedral epidote crystals.** The individual euhedral epidote crystals
583 clustering around the radial epidote aggregates (Figs. 1c, 2d, 2h and S1e) represent a final
584 stage of epidote crystallization. As shown by the experimental studies, polyhedral crystals are
585 produced with a small degree of supersaturation, slightly deviated from equilibrium state
586 (Lofgren 1974; Donaldson 1976; Fenn 1977; Oaki and Imai 2003). A low degree of
587 supersaturation sufficient to surmount the nucleation energy barrier for the formation of stable
588 crystal nuclei is required for the crystallization of these euhedral epidote grains (Vernon 2004).
589 Therefore, the individual epidote crystals around the epidote spherulites should have
590 crystallized at near equilibrium conditions upon a further decrease in supersaturation and a
591 further increase in the *D*/*G* ratio.

592 ## IMPLICATIONS

593 The fibrous crystals in the spherulites having relatively large interfacial energies would
594 recrystallize to adjust their shapes to equilibrium forms with low interfacial energies in a
595 protracted process. Such morphological adjustments of spherulites were observed in
596 experiments in which fibrous quartz and feldspar crystals growing from devitrified rhyolitic
597 glasses have locally recrystallized into an aggregate of fine equant grains (Lofgren 1971b).

598 Lofgren (1971b) envisioned that if the devitrification proceeds completely, a granophyric or
599 granitic texture forms without preservation of glassy precursors or spherulitic textures. In the
600 experiments of ammonium compound crystallization, dendritic ammonium thiocyanate
601 crystals formed in the initial stage of crystallization gradually changed into coarse-grained
602 euhedral crystals with prolonged crystallization time (1–50 h) under essentially constant
603 conditions (Means and Park 1994; Mills et al. 2011). The morphology of zirconia crystallized
604 from mixed solution of zirconium oxychloride and H_2SO_4 was primarily spherulitic in
605 short-duration runs while it changed into isolated and coarser crystals in longer duration runs
606 (Mottet et al. 1992). These observations mean that the non-equilibrium textures progressively
607 evolved towards equilibrium ones and will be eventually obliterated if the crystallization
608 conditions were kept constant for sufficient amounts of time. Thus, the preservation of the
609 epidote spherulites is possible only if they stay away from their crystallization conditions
610 rapidly, such as the quench processes of melts.

611 Quantitative modeling shows that the timescales for the growth of natural spherulites in
612 igneous rocks are on the orders of a few days or up to a few years, depending on temperature,
613 growth rate, and the size of the spherulites (Castro et al. 2008; Watkins et al. 2009; Von
614 Aulock et al. 2013; Bullock et al. 2017). Holding other parameters in equation (2) constant,
615 the $-\Delta G_r$ decreases and x increases as the system evolves towards equilibrium and the growth
616 rate decreases accordingly. A minimum growth rate (5.0×10^{-15} m·s^{-1}) is calculated by using
617 the conservative $-\Delta G_r$ ($0.4RT$) with a final average spherulite radius (x = 50 μm) in equation
618 (2). This minimum growth rate is 5×10^4 times lower than the conservative initial growth rate
619 (2.5×10^{-10} m·s^{-1}) estimated above as the final average radius of the epidote spherulites is the
620 same times larger than the assumed initial crystal nucleus. Dividing the final radius of the

spherulite by this minimum growth rate, an upper limit of the timescale for the spherulite growth is about 320 years. The actual timescale was likely smaller, in view of the conservative estimate of growth rate and the approximation of the spherulite by solid sphere. Therefore, the timescale for the crystallization of the epidote spherulites at Ganghe should be short and is incompatible with that of a protracted equilibrium but records a transient or dynamic process.

Short-lived metamorphism (from ~100 years up to <1 Ma) associated with pulsed fluid infiltration and/or heating was inferred from chromatographic modeling (Skelton, 2011) and diffusion modeling of oxygen and lithium isotopes and cations in metamorphic minerals (Young and Rumble III 1993; Van Haren et al. 1996; Graham et al. 1998; Camacho et al. 2005; Ague and Baxter 2007; Penniston-Dorland et al. 2010; Dragovic et al. 2015; Chu et al. 2017). Based on modeling of Sr diffusion in apatite and multicomponent diffusion in garnet, Ague and Baxter (2007) envisioned pulsed metamorphism in some of the mountain building processes. From the variations of epidote texture studied here, a similarly pulsed but much more short-lived metamorphic event may be inferred for the Ganghe metavolcanic breccia (Fig. 6b).

Based on the above considerations, it is suggested that the growth of epidote spherulites was due to *P*-*T* and fluid pulses followed by rapid restoring to ambient conditions. They were subjected to brittle deformation before being overgrown by the radial euhedral epidote aggregates (Figs. 2b–2d and 3b). The growth of this latter epidote texture was also a non-equilibrium process, and implies *P*-*T* and fluid pulses but a less degree of supersaturation/supercooling (Fig. 6b). If, as discussed above, their growth rate numerically equals the assumed diffusion rate of Al in a fluid ($D = 10^{-16}$ m$^2\cdot$s^{-1}, $D/G \approx 1$ m), the timescale

644 for the growth of 100 μm epidote crystals in these aggregate is about 3.2×10^4 years. The
645 crystallization of the individual euhedral epidote marks the restoring again to ambient
646 conditions.

647 Pulsed metamorphic events are suggested to be caused by shear heating or seismic faulting
648 (Camacho et al. 2005; Chu et al. 2017). The dynamic crystallization process responsible for
649 the rapid formation of the non-equilibrium epidote textures studied here may also be related to
650 seismicity (Austrheim & Andersen 2004; Petley-Ragan et al. 2018). Pseudotachylytes are
651 reported in the LGMRs in this area of Dabieshan, providing evidence for seismic events (Liu,
652 2002, Liu et al., 2005). The brittle deformation of the epidote spherulites (Figs. 2b–2d and 3b)
653 and the fragmentation of the radial euhedral epidote aggregates (Figs. 1c and 2g) imply
654 repeated tectonic brecciation in the metavolcanic breccia. The occurrence of the radial epidote
655 aggregates both in the fragments and in the matrix implies repeated growth of the textures.
656 The seismicity might have induced stress and fluid pulses in the wallrock (Sibson et al. 1975),
657 which may have caused the growth of the non-equilibrium epidote textures.

658 **ACKNOWLEDGEMENTS**

659 We thank Jay J. Ague, Stephen Centrella, two anonymous reviewers and the editors for
660 their constructive reviews and patient editorial handling, which greatly improved the
661 manuscript. Special thanks are due to Wen-Lan Zhang at Nanjing University for analyzing the
662 REE-bearing epidote by electron microprobe. We are also grateful to Qian Mao, Yu-Guang
663 Ma, Di Zhang and Juan Wang for help in the analysis of other minerals. Xin Yan and
664 Sai-Hong Yang helped in using the field emission scanning electron microscope. Chong Li
665 and Feng Nie assisted in the field. This work is supported by the National Natural Science
666 Foundation of China (Grant Nos. 41873040, 41573029 and 41490614).

REFERENCES CITED

Ague, J.J., and Baxter, E.F. (2007) Brief thermal pulses during mountain building recorded by Sr diffusion in apatite and multicomponent diffusion in garnet. Earth and Planetary Science Letters, 261, 500–516.

Ague, J.J. (2017) Element mobility during regional metamorphism in crustal and subduction zone environments with a focus on the rare earth elements (REE). American Mineralogist, 102, 1796–1821.

Austrheim, H., and Boundy, T.M. (1994) Pseudotachylytes generated during seismic faulting and eclogitization of the deep crust. Science, 265, 82–83.

Austrheim, H., and Andersen, T.B. (2004) Pseudotachylytes from Corsica: fossil earthquakes from a subduction complex. Terra Nova, 16, 193–197.

Austrheim, H. (2013) Fluid and deformation induced metamorphic processes around Moho beneath continent collision zones: examples from the exposed root zone of the Caledonian mountain belt, W-Norway. Tectonophysics, 609, 620–635.

Baker, D.R., and Freda, C. (2001) Eutectic crystallization in the undercooled Orthoclase-Quartz-H_2O system. European Journal of Mineralogy, 13, 453–466.

Barriga, F., and Fyfe, W. (1997) Multi-phase water-rhyolite interaction and ore fluid generation at Aljustrel, Portugal. Mineralium Deposita, 33, 188–207.

Befus, K.S., Watkins, J., Gardner, J.E., Richard, D., Befus, K.M., Miller, N.R., and Dingwell, D.B. (2015) Spherulites as in-situ recorders of thermal history in lava flows. Geology, 43, 647–650.

Blattner, P. (1976) Replacement of hornblende by garnet in granulite facies assemblages near Milford Sound, New Zealand. Contributions to Mineralogy and Petrology, 55, 181–190.

691 Brunsmann, A., Franz, G., Erzinger, J., and Landwehr, D. (2000) Zoisite-and
692 clinozoisite-segregations in metabasites (Tauern Window, Austria) as evidence for
693 high-pressure fluid-rock interaction. Journal of Metamorphic Geology, 18, 1–22.
694 Bullock, L.A., Gertisser, R., and O'Driscoll, B. (2017) Spherulite formation in obsidian lavas
695 in the Aeolian Islands, Italy. Periodico di Mineralogia, 86, 37–54.
696 Camacho, A., Lee, J.K., Hensen, B.J., and Braun, J. (2005) Short-lived orogenic cycles and
697 the eclogitization of cold crust by spasmodic hot fluids. Nature, 435, 1191–1196.
698 Carlson, W.D. (2010) Dependence of reaction kinetics on H_2O activity as inferred from rates
699 of intergranular diffusion of aluminium. Journal of Metamorphic Geology, 28, 735–752.
700 Carpenter, P.S., and Walker, N.W. (1992) Origin and tectonic significance of the Aldrich
701 Mountains serpentinite matrix melange, northeastern Oregon. Tectonics, 11, 690–708.
702 Castro, J.M., Beck, P., Tuffen, H., Nichols, A.R., Dingwell, D.B., and Martin, M.C. (2008)
703 Timescales of spherulite crystallization in obsidian inferred from water concentration
704 profiles. American Mineralogist, 93, 1816–1822.
705 Centrella, S., Austrheim, H., and Putnis, A. (2016) Mass transfer and trace element
706 redistribution during hydration of granulites in the Bergen Arcs, Norway. Lithos, 262, 1–10.
707 Centrella, S., Putnis, A., Lanari, P., and Austrheim, H. (2018) Textural and chemical evolution
708 of pyroxene during hydration and deformation: a consequence of retrograde metamorphism.
709 Lithos, 296–299, 245–264.
710 Chu, X., Ague, J.J., Podladchikov, Y.Y., and Tian, M. (2017) Ultrafast eclogite formation via
711 melting-induced overpressure. Earth and Planetary Science Letters, 479, 1–17.
712 Coggon, R., and Holland, T.J.B. (2002) Mixing properties of phengitic micas and revised
713 garnet-phengite thermobarometers. Journal of Metamorphic Geology, 20, 683–696.

Corrigan, G.M. (1982) The crystal morphology of plagioclase feldspar produced during isothermal supercooling and constant rate cooling experiments. Mineralogical Magazine, 46, 433–439.

Deer, W.A., Howie, R.A., and Zussman, J. (1986) Disilicates and ring silicates (Rock-forming minerals, volume 1B), 629 p. Longman, London.

Diener, J.F.A., Powell, R., White, R.W., and Holland, T.J.B. (2007) A new thermodynamic model for clino- and orthoamphiboles in the system Na2O-CaO-FeO-MgO-Al2O3-SiO2-H2O-O. Journal of Metamorphic Geology, 25, 631–656.

Dollase, W.A. (1971) Refinement of the crystal structures of epidote, allanite and hancockite. American Mineralogist, 56, 447–464.

Donaldson, C.H. (1976) An experimental investigation of olivine morphology. Contributions to Mineralogy and Petrology, 57, 187–213.

Dong, S.W., Oberhansli, R., Schmid, R., Liu, X.C., Tang, J.F., and Xue, H.M. (2002) Occurrence of metastable rocks in deeply subducted continental crust from the Dabie Mountains, central China. Episodes, 25, 84–89.

Dragovic, B., Baxter, E.F., and Caddick, M.J. (2015) Pulsed dehydration and garnet growth during subduction revealed by zoned garnet geochronology and thermodynamic modeling, Sifnos, Greece. Earth and Planetary Science Letters, 413, 111–122.

Droop, G. (1987) A general equation for estimating Fe^{3+} concentrations in ferromagnesian silicates and oxides from microprobe analyses, using stoichiometric criteria. Mineralogical Magazine, 51, 431–435.

Etheridge, M., Wall, V., and Vernon, R. (1983) The role of the fluid phase during regional

metamorphism and deformation. Journal of Metamorphic Geology, 1, 205–226.

Feldman, V.I. (1994) The conditions of shock metamorphism. Geological Society of America Special Papers, 293, 121–132.

Fenn, P.M. (1977) The nucleation and growth of alkali feldspars from hydrous melts. The Canadian Mineralogist, 15, 135–161.

Finger, F., Broska, I., Roberts, M.P., and Schermaier, A. (1998) Replacement of primary monazite by apatite-allanite-epidote coronas in an amphibolite facies granite gneiss from the eastern Alps. American Mineralogist, 83, 248–258.

Frei, D., Liebscher, A., Wittenberg, A., and Shaw, C.S. (2003) Crystal chemical controls on rare earth element partitioning between epidote-group minerals and melts: an experimental and theoretical study. Contributions to Mineralogy and Petrology, 146, 192–204.

Gardner, J.E., Befus, K.S., Watkins, J., Hesse, M., and Miller, N. (2012) Compositional gradients surrounding spherulites in obsidian and their relationship to spherulite growth and lava cooling. Bulletin of Volcanology, 74, 1865–1879.

Graham, C.M., Valley, J.W., Eiler, J.M., and Wada, H. (1998) Timescales and mechanisms of fluid infiltration in a marble: an ion microprobe study. Contributions to Mineralogy and Petrology, 132, 371–389.

Gránásy, L., Rátkai, L., Szállás, A., Korbuly, B., Tóth, G.I., Környei, L., and Pusztai, T. (2014) Phase-field modeling of polycrystalline solidification: from needle crystals to spherulites—A review. Metallurgical and Materials Transactions A, 45, 1694–1719.

Green, E., Holland, T.J.B., and Powell, R. (2007) An order-disorder model for omphacitic pyroxenes in the system jadeite-diopside-hedenbergite-acmite, with applications to eclogitic rocks. American Mineralogist, 92, 1181–1189.

760 Guo, S., Ye, K., Chen, Y., Liu, J.B., Mao, Q., and Ma, Y.G. (2012) Fluid–rock interaction and
761 element mobilization in UHP metabasalt: constraints from an omphacite–epidote vein and
762 host eclogites in the Dabie orogen. Lithos, 136, 145–167.
763 Halcrow, H.M. (1956) The geology of Waiheke Island, Auckland. Transactions of the Royal
764 Society of New Zealand, 84, 51–69.
765 Harper, G.D. (1995) Pumpellyosite and prehnitite associated with epidosite in the Josephine
766 Ophiolite—Ca metasomatism during upwelling of hydrothermal fluids at a spreading axis.
767 Geological Society of America Special Papers, 296, 101–122.
768 Heinrich, E.W. (1964) Notes on western mineral occurrences: 3, thulite from Camp Creek,
769 Ruby Mountains, Montana; 4, hypersthene veinlets, Timber Gulch, Ruby Mountains,
770 Montana. American Mineralogist, 49, 430–435.
771 Holland, T.J.B., and Powell, R. (2003) Activity-composition relations for phases in
772 petrological calculations: an asymmetric multicomponent formulation. Contributions to
773 Mineralogy and Petrology, 145, 492–501.
774 Holland, T.J.B., and Powell, R. (2011) An improved and extended internally consistent
775 thermodynamic dataset for phases of petrological interest, involving a new equation of state
776 for solids. Journal of Metamorphic Geology, 29, 333–383.
777 Hudson, S.N. (1937) The volcanic rocks and minor intrusions of the Cross Fell Inlier,
778 Cumberland and Westmorland. Quarterly Journal of the Geological Society, 93, 368-405.
779 John, T., and Schenk, V. (2006) Interrelations between intermediate-depth earthquakes and
780 fluid flow within subducting oceanic plates: constraints from eclogite facies
781 pseudotachylytes. Geology, 34, 557–560.
782 Jones, B. (2017) Review of aragonite and calcite crystal morphogenesis in thermal spring

783 systems. Sedimentary Geology, 354, 9–23.
784 Keith, H.D., and Padden, F.J. (1963) A phenomenological theory of spherulitic crystallization.
785 Journal of Applied Physics, 34, 2409–2421.
786 Kirkpatrick, R.J. (1981) Kinetics of crystallization of igneous rocks. Reviews in Mineralogy,
787 8, 321–395.
788 Kitchen, D. (1985) The parental magma on Rhum: evidence from alkaline segregations and
789 veins in the peridotites from Salisbury's Dam. Geological Magazine, 122, 529–537.
790 Lanari, P., and Engi, M. (2017) Local bulk composition effects on metamorphic mineral
791 assemblages. Reviews in Mineralogy and Geochemistry, 83, 55–102.
792 Lin, A. (2008) Fossil earthquakes: the formation and preservation of pseudotachylytes, 348 p.
793 Springer, Berlin Heidelberg.
794 Liu, J.M. (2002) Origin of pseudotachylite from the eastern Dabieshan orogenic belt and its
795 tectonic implications, 86 p. Ph.D. thesis, Chinese Academy of Geological Sciences, Beijing,
796 China (in Chinese with English abstract).
797 Liu, J.M., Dong, S.W., Zhang, J.S., Liu, X.C., and Chen, B.L. (2005) Microstructure
798 characteristics of pseudotachylites from the eastern Dabieshan orogenic belt and their
799 tectonic implications. Acta Geoscientica Sinica, 263, 229–234 (in Chinese with English
800 abstract).
801 Lofgren, G. (1971a) Spherulitic textures in glassy and crystalline rocks. Journal of
802 Geophysical Research, 76, 5635–5648.
803 Lofgren, G. (1971b) Experimentally produced devitrification textures in natural rhyolitic glass.
804 Geological Society of America Bulletin, 82, 111–124.
805 Lofgren, G. (1974) An experimental study of plagioclase crystal morphology: isothermal

806 crystallization. American Journal of Science, 274, 243–273.
807 Lofgren, G., (1980). Experimental studies on the dynamic crystallization of silicate melts. In
808 R.B. Hargraves Ed., Physics of Magmatic Processes, p. 487–551. Princeton University
809 Press, Princeton, New Jersey.
810 Magill, J., and Plazek, D. (1967) Physical properties of aromatic hydrocarbons. II.
811 solidification behavior of 1, 3, 5-Tri-α-naphthylbenzene. The Journal of Chemical Physics,
812 46, 3757–3769.
813 McCann, A., and Kennedy, M. (1974) A probable glacio-marine deposit of Late
814 Ordovician—Early Silurian age from the north central Newfoundland Appalachian Belt.
815 Geological Magazine, 111, 549–564.
816 Means, W., and Park, Y. (1994) New experimental approach to understanding igneous texture.
817 Geology, 22, 323–326.
818 Melinger-Cohen, A.Z., Bina, C.R., and Jacobsen, S.D. (2015) A petrologic model for
819 hydrothermal metamorphism in the Portage Lake volcanic series, northern Michigan.
820 Northwestern Undergraduate Research Journal, http://www.thenurj.com/theses.
821 Mills, R.D., Ratner, J.J., and Glazner, A.F. (2011) Experimental evidence for crystal
822 coarsening and fabric development during temperature cycling. Geology, 39, 1139–1142.
823 Minakawa, T., Fukushima, H., Nishio-Hamane, D., and Miura, H. (2008) Epidote-(Sr),
824 $CaSrAl_2Fe^{3+}(Si_2O_7)(SiO_4)(OH)$, a new mineral from the Ananai mine, Kochi Prefecture,
825 Japan. Journal of Mineralogical and Petrological Sciences, 103, 400–406.
826 Misch, P. (1965) Radial epidote glomeroblasts formed under conditions of synkinematic
827 metamorphism—A new mechanism of collective crystalloblastesis. Geologische
828 Rundschau, 54, 944–956.

Monecke, T., Renno, A.D., and Herzig, P.M. (2004) Primary clinopyroxene spherulites in basaltic lavas from the Pacific–Antarctic Ridge. Journal of Volcanology and Geothermal Research, 130, 51–59.

Mottet, B., Pichavant, M., Bény, J.M., and Alary, J.A. (1992) Morphology of zirconia synthesized hydrothermally from zirconium oxychloride. Journal of the American Ceramic Society, 75, 2515–2519.

Nakamura, Y., Oohashi, K., Toyoshima, T., Satish-Kumar, M., and Akai, J. (2015) Strain-induced amorphization of graphite in fault zones of the Hidaka metamorphic belt, Hokkaido, Japan. Journal of Structural Geology, 72, 142–161.

Nehlig, P., and Juteau, T. (1988) Flow porosities, permeabilities and preliminary data on fluid inclusions and fossil thermal gradients in the crustal sequence of the Sumail ophiolite (Oman). Tectonophysics, 151, 199–221.

Oaki, Y., and Imai, H. (2003) Experimental demonstration for the morphological evolution of crystals grown in gel media. Crystal Growth & Design, 3, 711–716.

Owens, B.E., and Dymek, R.F. (2016) Comparative Petrology of the Montpelier and Roseland Potassic Anorthosites, Virginia. The Canadian Mineralogist, 54, 1563–1593.

Pascual, F.J.R., Matas, J., and Parra, L.M.M. (2013) High-pressure metamorphism in the Early Variscan subduction complex of the SW Iberian Massif. Tectonophysics, 592, 187–199.

Pattison, D.R.M., De Capitani, C., and Gaidies, F. (2011) Petrological consequences of variations in metamorphic reaction affinity. Journal of Metamorphic Geology, 29, 953–977.

Penniston-Dorland, S.C., Sorensen, S.S., Ash, R.D., and Khadke, S.V. (2010) Lithium isotopes as a tracer of fluids in a subduction zone mélange: Franciscan Complex, CA. Earth

and Planetary Science Letters, 292, 181–190.

Petley-Ragan, A., Dunkel, K.G., Austrheim, H., Ildefonse, B., and Jamtveit, B. (2018) Microstructural records of earthquakes in the lower crust and associated fluid-driven metamorphism in plagioclase-rich granulites. Journal of Geophysical Research: Solid Earth, 123, 3729–3746.

Powell, R., Holland, T., and Worley, B. (1998) Calculating phase diagrams involving solid solutions via non-linear equations, with examples using THERMOCALC. Journal of Metamorphic Geology, 16, 577–588.

Putnis, A., Jamtveit, B., and Austrheim, H. (2017) Metamorphic processes and seismicity: the Bergen Arcs as a natural laboratory. Journal of Petrology, 58, 1871–1898.

Rebay, G., and Messiga, B. (2007) Prograde metamorphic evolution and development of chloritoid-bearing eclogitic assemblages in subcontinental metagabbro (Sesia–Lanzo zone, Italy). Lithos, 98, 275–291.

Ridley, J., and Thompson, A. (1986) The role of mineral kinetics in the development of metamorphic microtextures. Advances in Physical Geochemistry, 5, 154–193.

Ross, C.S. (1941) Occurrence and origin of the titanium deposits of Nelson and Amherst Counties, Virginia. United States Geological Survey Professional Paper, 198, 59p..

Rubie, D.C. (1986) The catalysis of mineral reactions by water and restrictions on the presence of aqueous fluid during metamorphism. Mineralogical Magazine, 50, 399–415.

Rubie, D.C. (1998) Disequilibrium during metamorphism: the role of nucleation kinetics. Geological Society, London, Special Publications, 138, 199–214.

Saito, Y., and Ueta, T. (1989) Monte Carlo studies of equilibrium and growth shapes of a crystal. Physical Review A, 40, 3408–3419.

875 Schmid, R., Romer, R.L., Franz, L., Oberhansli, R., and Martinotti, G. (2003) Basement-cover
876 sequences within the UHP unit of the Dabie Shan. Journal of Metamorphic Geology, 21,
877 531–538.
878 Shtukenberg, A.G., Punin, Y.O., Gunn, E., and Kahr, B. (2011) Spherulites. Chemical
879 Reviews, 112, 1805–1838.
880 Sibson, R., Moore, J.M.M., and Rankin, A. (1975) Seismic pumping—a hydrothermal fluid
881 transport mechanism. Journal of the Geological Society, 131, 653–659.
882 Skelton, A. (2011) Flux rates for water and carbon during greenschist facies metamorphism.
883 Geology, 39, 43–46.
884 Soule, S.A., Fornari, D.J., Perfit, M.R., Ridley, W.I., Reed, M.H., and Cann, J.R. (2006)
885 Incorporation of seawater into mid-ocean ridge lava flows during emplacement. Earth and
886 Planetary Science Letters, 252, 289–307.
887 Stout, M.L. (1964) Geology of a part of the south-central Cascade Mountains, Washington.
888 Geological Society of America Bulletin, 75, 317–334.
889 Stuart-Smith, P. (1990) Evidence for extensional tectonics in the Tumut trough, Lachlan fold
890 belt, NSW. Australian Journal of Earth Sciences, 37, 147–167.
891 Su, W.H., Liu, S.E., Xu, D.P., Wang, W.R., Yao, B., Liu, X.M., Liu, Z.G., and Zhong, Z. (2006)
892 Effects of local mechanical collision with shear stress on the phase transformation from
893 α-quartz to coesite induced by high static pressure. Physical Review B, 73, 144110, DOI:
894 10.1103/PhysRevB.73.144110.
895 Sunagawa, I. (1999) Growth and morphology of crystals. Forma, 14, 147–166.
896 Torres-Alvarado, I.S. (2002) Chemical equilibrium in hydrothermal systems: the case of Los
897 Azufres geothermal field, Mexico. International Geology Review, 44, 639–652.

898 Van Haren, J.L., Ague, J.J., and Rye, D.M. (1996) Oxygen isotope record of fluid infiltration
899 and mass transfer during regional metamorphism of pelitic schist, Connecticut, USA.
900 Geochimica et Cosmochimica Acta, 60, 3487–3504.
901 Van Staal, C.R., Ravenhurst, C.E., Winchester, J.A., Roddick, J.C., and Langton, J.P. (1990)
902 Post-Taconic blueschist suture in the northern Appalachians of northern New Brunswick,
903 Canada. Geology, 18, 1073–1077.
904 Vernon, R.H. (2004) A practical guide to rock microstructure, 578 p. Cambridge University
905 Press, New York.
906 Von Aulock, F., Nichols, A., Kennedy, B., and Oze, C. (2013) Timescales of texture
907 development in a cooling lava dome. Geochimica et Cosmochimica Acta, 114, 72–80.
908 Walther, J.V., and Wood, B.J. (1984) Rate and mechanism in prograde metamorphism.
909 Contributions to Mineralogy and Petrology, 88, 246–259.
910 Watkins, J., Manga, M., Huber, C., and Martin, M. (2009) Diffusion-controlled spherulite
911 growth in obsidian inferred from H_2O concentration profiles. Contributions to Mineralogy
912 and Petrology, 157, 163–172.
913 White, R.W., Powell, R., and Holland, T.J.B. (2007) Progress relating to calculation of partial
914 melting equilibria for metapelites. Journal of Metamorphic Geology, 25, 511–527.
915 Whitney, D.L., and Evans, B.W. (2010) Abbreviations for names of rock-forming minerals.
916 American Mineralogist, 95, 185–187.
917 Wilbur, D.E., and Ague, J.J. (2006) Chemical disequilibrium during garnet growth: Monte
918 Carlo simulations of natural crystal morphologies. Geology, 34, 689–692.
919 Xu, Q.D., and Scott, S.D. (2005) Spherulitic pyrite in seafloor hydrothermal deposits:
920 products of rapid crystallization from mixing fluids. In J. W. Mao and P. Frank, Eds.,

921 Mineral Deposit Research: Meeting the Global Challenge: Proceedings of the Eighth
922 Biennial SGA Meeting, p. 711–713. Springer, Berlin Heidelberg.
923 Yang, J.J., Fan, Z.F., Yu, C., and Yan, R. (2014a) Coseismic formation of eclogite facies
924 cataclasite dykes at Yangkou in the Chinese Su-Lu UHP metamorphic belt. Journal of
925 Metamorphic Geology, 32, 937–960.
926 Yang, J.J., Huang, M.X., Wu, Q.Y., and Zhang, H.R. (2014b) Coesite-bearing eclogite breccia:
927 implication for coseismic ultrahigh-pressure metamorphism and the rate of the process.
928 Contributions to Mineralogy and Petrology, 167, DOI: 10.1007/s00410-014-1013-7.
929 Yang, J.J., Zhang, H.R., Chen, A.P., and Huang, M.X. (2017) Petrological evidence for
930 shock-induced high-P metamorphism in a gabbro. Journal of Metamorphic Geology, 35,
931 121–140.
932 Young, E.D., and Rumble III, D. (1993) The origin of correlated variations in in-situ $^{18}O/^{16}O$
933 and elemental concentrations in metamorphic garnet from southeastern Vermont, USA.
934 Geochimica et Cosmochimica Acta, 57, 2585–2597.
935 Zhang, R.Y., Liou, J.G., and Ernst, W.G. (2009) The Dabie–Sulu continental collision zone: a
936 comprehensive review. Gondwana Research, 16, 1–26.
937 Zheng, Y.F., Fu, B., Gong, B., and Li, L. (2003) Stable isotope geochemistry of ultrahigh
938 pressure metamorphic rocks from the Dabie–Sulu orogen in China: implications for
939 geodynamics and fluid regime. Earth-Science Reviews, 62, 105–161.
940 Zheng, Y.F., Zhou, J.B., Wu, Y.B., and Xie, Z. (2005) Low-grade metamorphic rocks in the
941 Dabie-Sulu orogenic belt: a passive-margin accretionary wedge deformed during continent
942 subduction. International Geology Review, 47, 851–871.
943 Zhou, J.B., Zheng, Y.F., Li, L., and Xie, Z. (2001) On low-grade metamorphic rocks within

944 Dabie-Sulu ultra-high pressure metamorphic belt. Acta Petrologica Sinica, 17, 39–48 (in
945 Chinese with English abstract).
946

This is a preprint, the final version is subject to change, of the American Mineralogist (MSA)
Cite as Authors (Year) Title. American Mineralogist, in press.
DOI: https://doi.org/10.2138/am-2019-6980

947 # FIGURE CAPTIONS

948 **Figure 1**

949 **(a)** Contact relationship between the metavolcanic breccia (MB) and the enclosed
950 coesite-bearing eclogite (CE) body, which is about 8 m in length and 50 cm in width. Their
951 boundary is outlined with a white line. The dashed lines on the upper left represent inferred
952 boundary covered by soil.

953 **(b)** A polished hand specimen of the metavolcanic breccia consisting of various types of
954 volcanic fragments with variable shapes and sizes in a fine-grained matrix. An albitophyre
955 fragment (A) and a hematite rich fragment (F) are labelled.

956 **(c)** Backscattered electron image of a fragment dominated by phengite and epidote, with
957 less amounts of garnet and Na-plagioclase and several pseudomorphs after igneous
958 plagioclase (Pl ps), is outlined by a white dashed line. Some skeletal garnet grains are
959 arrowed. Radial euhedral epidote aggregates occur both in the fragment and in the matrix
960 (upper right, arrowed). Many of the radial epidote aggregates on the border of the fragment
961 are cut off and only parts of them are left in the fragment.

962

963 **Figure 2** Photomicrographs and backscattered electron (BSE) images of epidote textures in
964 the metavolcanic breccia. Solid circles mark the spots of electron microprobe analysis and the
965 numbers correspond to the data number in Table 1.

966 **(a)** Photomicrograph of a fan-shaped epidote spherulite in the matrix (cross-polarized light).
967 The spherulite is overgrown by discrete epidote grains and is further surrounded by the
968 fine-grained matrix minerals including plagioclase, K-feldspar, phengite, biotite, quartz,
969 garnet and hematite. The epidote fibers in the spherulite display sweeping extinctions.

970 **(b)** BSE image of a spherulite consisting of bright (REE-rich) epidote fibers and dark
971 (REE-poor) interfibrillar epidote. The fibers become finer away from the radiating point. Low
972 angle non-crystallographic branching can be seen. REE concentration shows a general
973 decrease away from the radiating point. The intervening lath-shaped epidote crystals
974 (indicated by arrows) overgrowing the spherulite are similarly variable in REE contents
975 across their boundaries. REE-poor epidote grains appear as inclusions in the spherulite. The
976 area around the radiating point is fragmented. The whole texture may be viewed to be a
977 portion of a fragmented original spherulite.
978 **(c)** BSE image of an epidote spherulite with REE-rich epidote fibers concentrated and
979 radiating from the center, setting in a matrix composed of plagioclase, biotite, K-feldspar,
980 quartz, phengite, garnet and hematite. Some of these minerals are enclosed in the zone
981 between the spherulite and the lath-shaped epidote overgrowth (middle left). In the central
982 part of the texture, the spherulite is fragmented, with randomly oriented bits of the bright
983 fibrous epidote cemented by dark epidote. The overgrowing radiating epidote laths are further
984 overgrown by euhedral epidote crystals displaying faint oscillatory zoning and bright rims
985 (lower middle). These overgrowths on the spherulite remain integrate, implying that the
986 fragmentation of the spherulite predates the overgrowths.
987 **(d)** BSE image of broken epidote spherulites overgrown by REE-poor epidote radiating in
988 the same directions of the epidote fibers. The cores of the spherulites are more intensively
989 fragmented and are cemented by REE-poor epidote. Fine-grained hematite (arrowed) and
990 zircon (in black circles) are included both in the spherulitic parts and in the cementing epidote.
991 The matrix is a fine-grained assemblage of Qz + Na-Pl + Ph + Kfs + Ep + Grt + Hem.
992 **(e)** Enlarged view of a large fragment of the spherulite on the right part of Fig. 3d, the

993 REE-rich epidote fibers are branching and are terminated by euhedral epidote (arrowed).
994 **(f)** Photomicrograph of radial euhedral epidote aggregates in a fragment dominated by
995 fine-grained phengite and epidote (cross-polarized light).
996 **(g)** BSE image of two radial aggregates of euhedral epidote around randomly oriented
997 epidote grains in the matrix of a fragment. The epidote crystals display oscillatory zoning with
998 alternating bright and dark zones mimicking the euhedral shapes of the crystals. The epidote
999 grains overgrew or indent the matrix minerals.
1000 **(h)** BSE image of a spherical aggregate of euhedral epidote crystals radiating around quartz
1001 and plagioclase in a matrix of biotite, garnet, quartz, plagioclase, phengite, hematite and
1002 K-feldspar. Individual epidote grains in the aggregate are zoned in composition, with their
1003 brighter tips and margins higher in Fe than the darker inner parts. The biotite flake on the
1004 upper left is indented by the epidote grain. Garnet and phengite appear as interstitial grains
1005 between in the epidote crystals.
1006
1007 **Figure 3** Backscattered electron images showing the relationship between the orientations of
1008 the crystals in the spherulite texture and the foliation (indicated by double-headed arrows).
1009 **(a)** An epidote spherulite growing over the foliation formed by the matrix minerals (Pl + Qz
1010 + Kfs + Ph + Bt + Ep + Grt + Ttn + Hem) in a lithic fragment. The orientations of the epidote
1011 fibers in the spherulite are at a large angle to the foliation. An elliptical epidote aggregate
1012 enclosing the matrix minerals occurs on the left side.
1013 **(b)** An enlarged view of part of the epidote spherulite in (a) showing inclusions of quartz
1014 (arrowed) rimmed by epidote in the core (lower left) and inclusions of biotite, phengite and
1015 quartz in the zone in the spherulite and the overgrowing epidote. The core of the spherulite is

fragmented, with the bright bits of epidote cemented by dark epidote. The epidote crystals extending from the epidote fibers truncate the foliation formed by oriented phengite, biotite and hematite in the matrix. The phengite flakes appear to be overgrown by the epidote laths.

(c) An epidote aggregate between a fine-grained fragment in the lower left and the coarser-grained matrix (Pl + Qz + Kfs + Ph + Bt + Ep + Grt + Ttn + Hem). The fragment contains more abundant hematite and plagioclase and the matrix is more abundant in phengite and quartz. The foliation runs through both of them in the lower left to upper right direction. The difference in mineral assemblage and the same foliation suggest that both the volcanic lithic fragment and the matrix were subjected to greenschist facies metamorphism.

(d) An enlarged view of an epidote spherulite on the right side of the epidote aggregate in (c) showing a broken epidote spherulite (bright epidote) overgrown by dark epidote grains. The central area is a mixture of many fine-grained, randomly oriented bright bits of epidote (one of them is arrowed) with coarser dark epidote grains. The missing parts of the spherulite on the upper right and lower left as well as the flow pattern of the bright bit of epidote in the central area suggests that the fragmentation was coeval with foliation. A large part of the broken spherulite on the right and a dendritic part on the lower right are magnified in Fig. 2e and Fig. S1c, respectively.

Figure 4 REE-Al plot showing the composition of epidote in spherulites, radial euhedral epidote aggregates (REEA) and individual euhedral epidote grains.

Figure 5

(a) Thermobarometry for the matrix assemblage of the metavolcanic breccia (Pl + Kfs + Ph

+ Ep +Bt + Grt + Hem + Sph + Qz). Intersections of the selected equilibria yield *P*-*T* estimates of 5.5–6 kbar and 475–485 °C.

(b) *T*-$\log_{10}(fO_2)$ diagram (*P* = 6 kbar) calculated with the same assemblage used in (a). The intersections selected of O_2-bearing equilibria yield the $\log_{10}(fO_2)$ ranging from −22.7 to −22.4. The NNO (Ni-NiO) and MH (magnetite-hematite) buffers are calculated at the same pressure for comparison.

(c) *P*-*T* pseudosection of plagioclase pseudomorph in the metavolcanic breccia, with H_2O, quartz and phengite in excess. The bulk composition is (in mol%): SiO_2 (69.74), Al_2O_3 (15.77), CaO (3.27), MgO (0.33), FeO (0.91), K_2O (2.17), Na_2O (7.60), and Fe_2O_3 (0.21). The dotted and dashed lines in the field of Pl + Ph + Ep + Qz + H_2O signify isopleths of anorthite end-member proportion in the plagioclase (X_{An}) and paragonite end-member proportion in the phengite (X_{Pg}), respectively. The ranges of the X_{An} (0.08–0.10) and X_{Pg} (0.034–0.040) correspond to a *P*-*T* range of 435 °C to 515 °C and 5 kbar to 7 kbar (shaded quadrilateral).

(d) *P*-*M*(H_2O) pseudosection calculated at 450 °C, with the relative proportion of the oxides other than H_2O being the same with Fig. 5a. Quartz and phengite are present in all of the assemblages unless those at low *M*(H_2O) labelled with '−Ph', which means the absence of phengite. The thick line indicates the H_2O-saturation and dotted lines signify the isopleth of X_{An}. The regions of the observed assemblages (Pl + Ph + Ep ± Kfs ± Qz) are shaded.

Figure 6

(a) Inferred pressure (*P*)-temperature (*T*) path followed by the metavolcanic breccia during the crystallization of a radial epidote aggregate. The *P*-*T*-fluid pulse is thought to have been induced by faulting, forming the *P*-*T* loop (dotted lines) from the ambient conditions (shaded

quadrilateral) corresponding to greenschist facies conditions. The epidote spherulites or the radial euhedral epidote aggregates crystallized as the *P*-*T* conditions rapidly restored from the *P*-*T* spike to the ambient conditions. The equilibria Ab = Jd + Qz and Kfs + 4An + $2H_2O$ = 2Qz + Ms + 2Zo are plotted to constrain the possible range of the *P*-*T* spike. As quantitative *P*-*T* estimates for the spherulites are difficult to make, *P*-*T* values of the spike are only shown for schematic illustration. See text for discussion on the uncertainty arisen from that of the *P*-*T* spike.

(b) Schematic illustration showing the *P*-*T* variations of the metavolcanic breccia with time (*t*). The spherulites may have crystallized in response to the first larger *P*-*T*-fluid pulse. The radial euhedral epidote aggregates (REEA) crystallized subsequent to brecciation of the epidote spherulite, in response to the second smaller *P*-*T* pulse. The individual euhedral epidote crystals surrounding the epidote spherulites and the radial euhedral epidote aggregates crystallized as the *P*-*T* restored to the ambient greenschist facies conditions.

TABLES

Table 1 Representative electron microprobe analyses of epidote in different epidote textures.

Table 2 Representative electron microprobe analyses of minerals in the matrix.

Table 3 Representative electron microprobe analyses of minerals in the plagioclase pseudomorphs.

This is a preprint, the final version is subject to change, of the American Mineralogist (MSA)
Cite as Authors (Year) Title. American Mineralogist, in press.
DOI: https://doi.org/10.2138/am-2019-6980

Figure 1

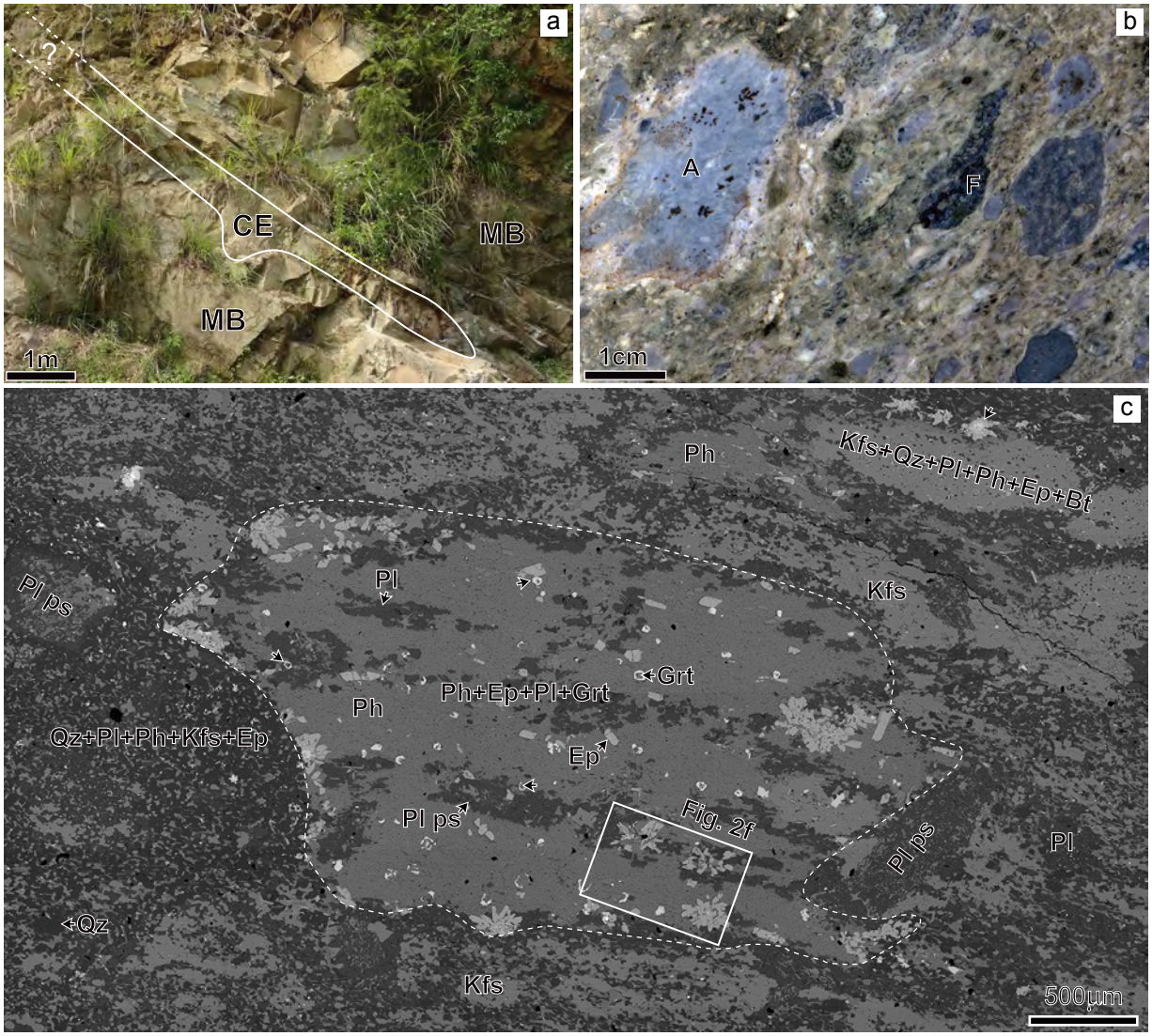

This is a preprint, the final version is subject to change, of the American Mineralogist (MSA)
Cite as Authors (Year) Title. American Mineralogist, in press.
DOI: https://doi.org/10.2138/am-2019-6980

Figure 2

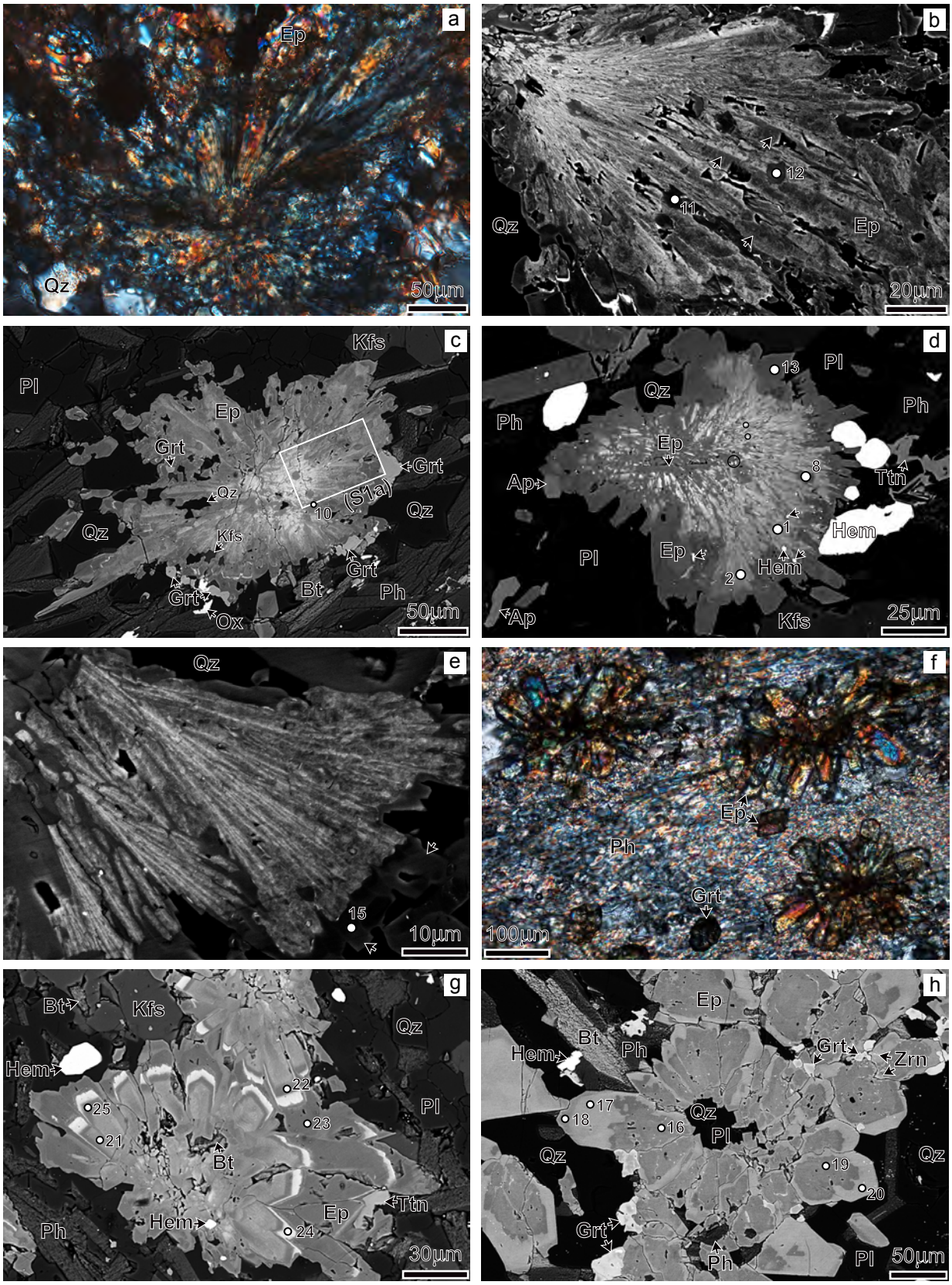

This is a preprint, the final version is subject to change, of the American Mineralogist (MSA)
Cite as Authors (Year) Title. American Mineralogist, in press.
DOI: https://doi.org/10.2138/am-2019-6980

Figure 3

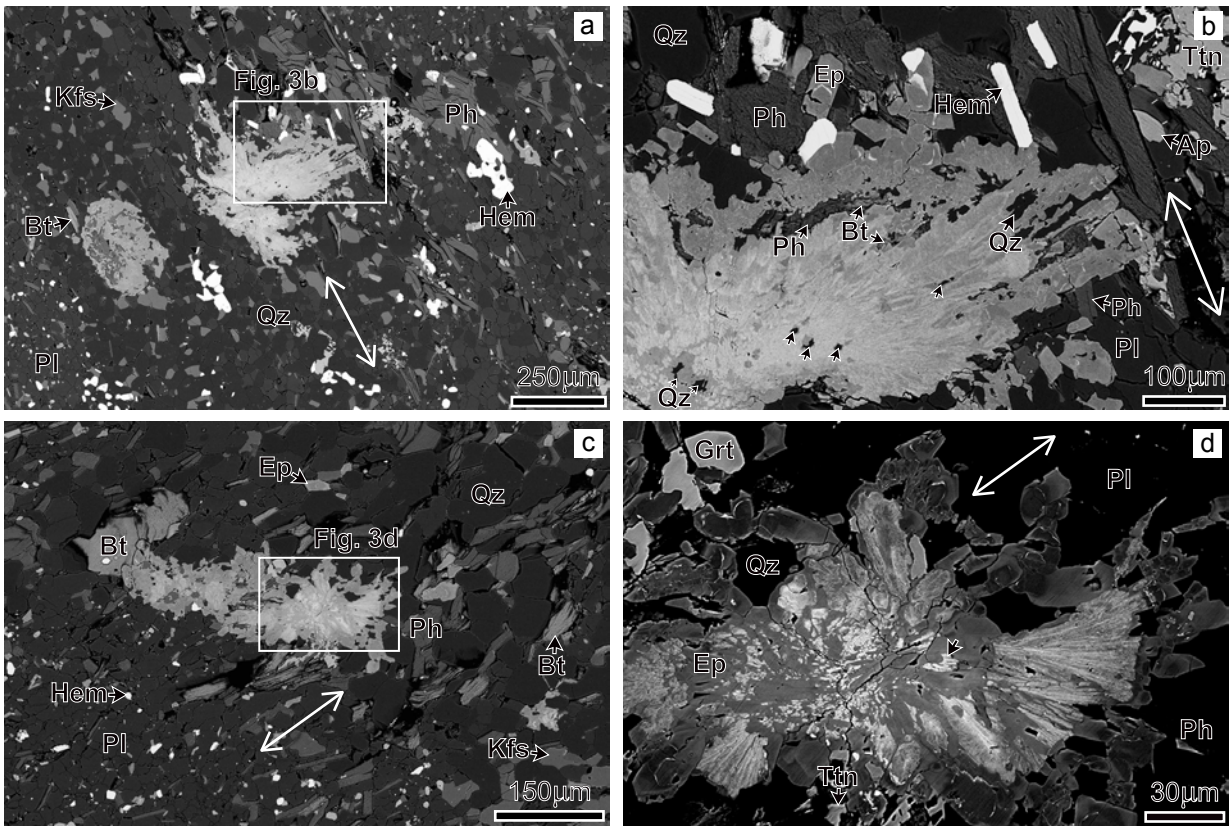

This is a preprint, the final version is subject to change, of the American Mineralogist (MSA)
Cite as Authors (Year) Title. American Mineralogist, in press.
DOI: https://doi.org/10.2138/am-2019-6980

Figure 4

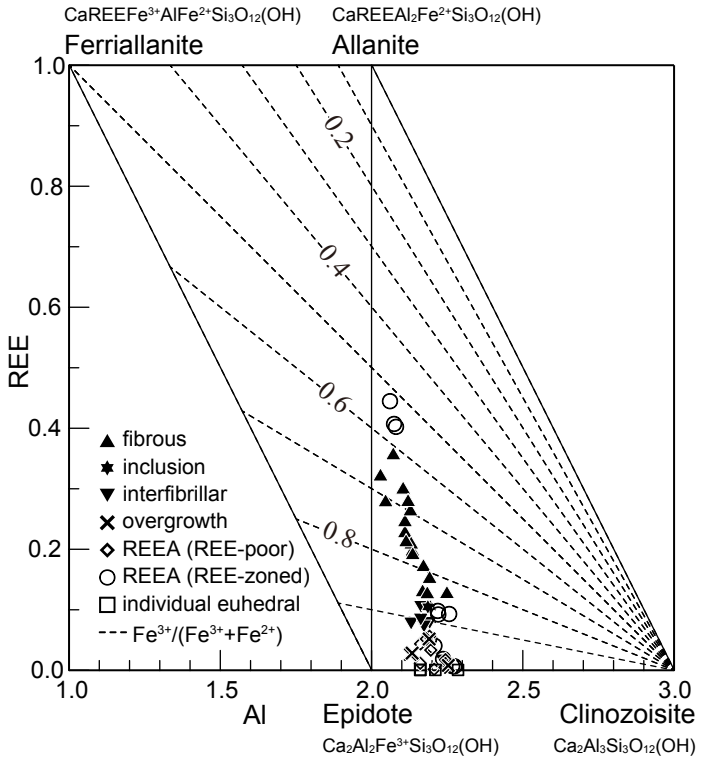

This is a preprint, the final version is subject to change, of the American Mineralogist (MSA)
Cite as Authors (Year) Title. American Mineralogist, in press.
DOI: https://doi.org/10.2138/am-2019-6980

Figure 5

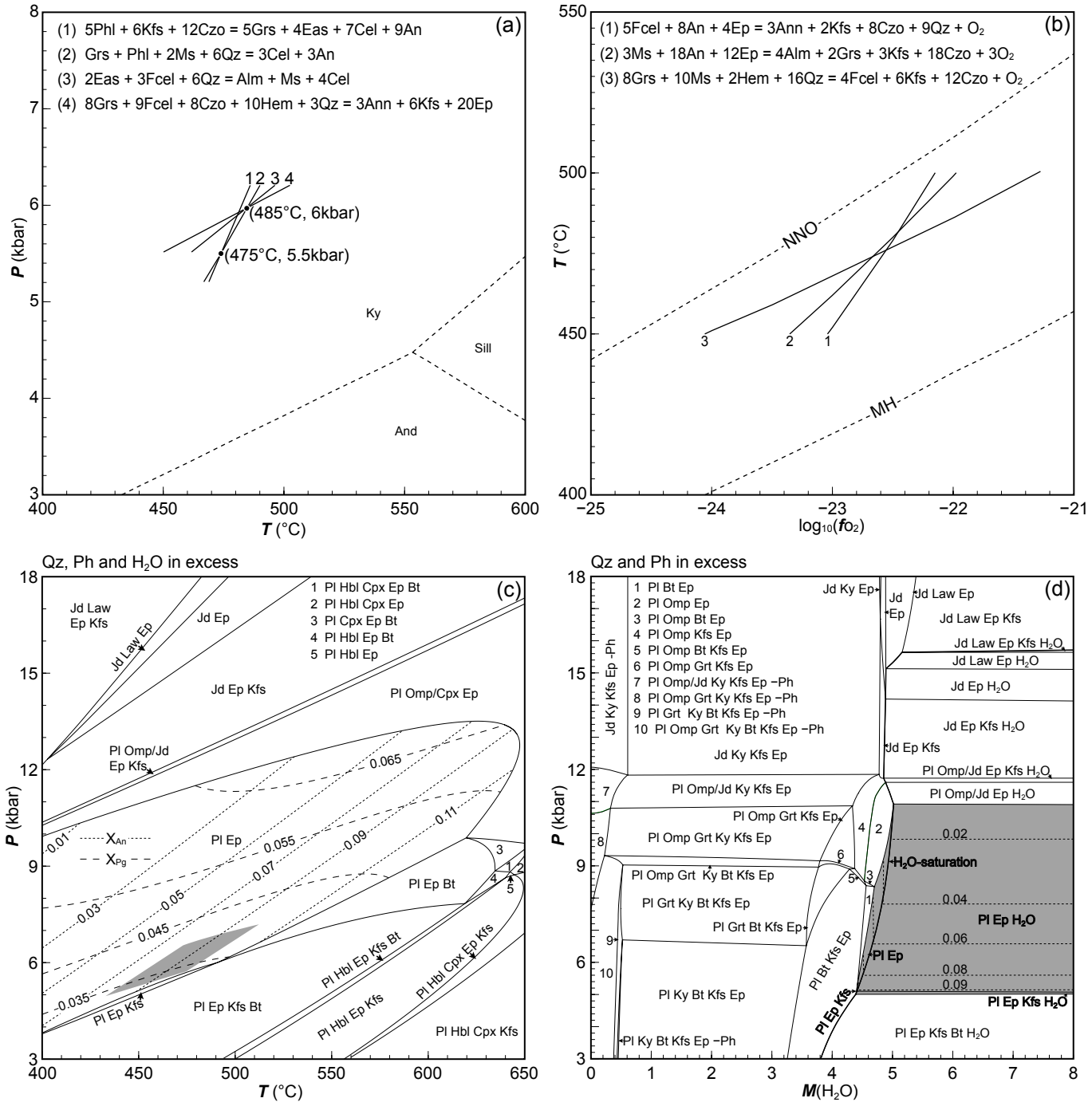

This is a preprint, the final version is subject to change, of the American Mineralogist (MSA)
Cite as Authors (Year) Title. American Mineralogist, in press.
DOI: https://doi.org/10.2138/am-2019-6980

Figure 6

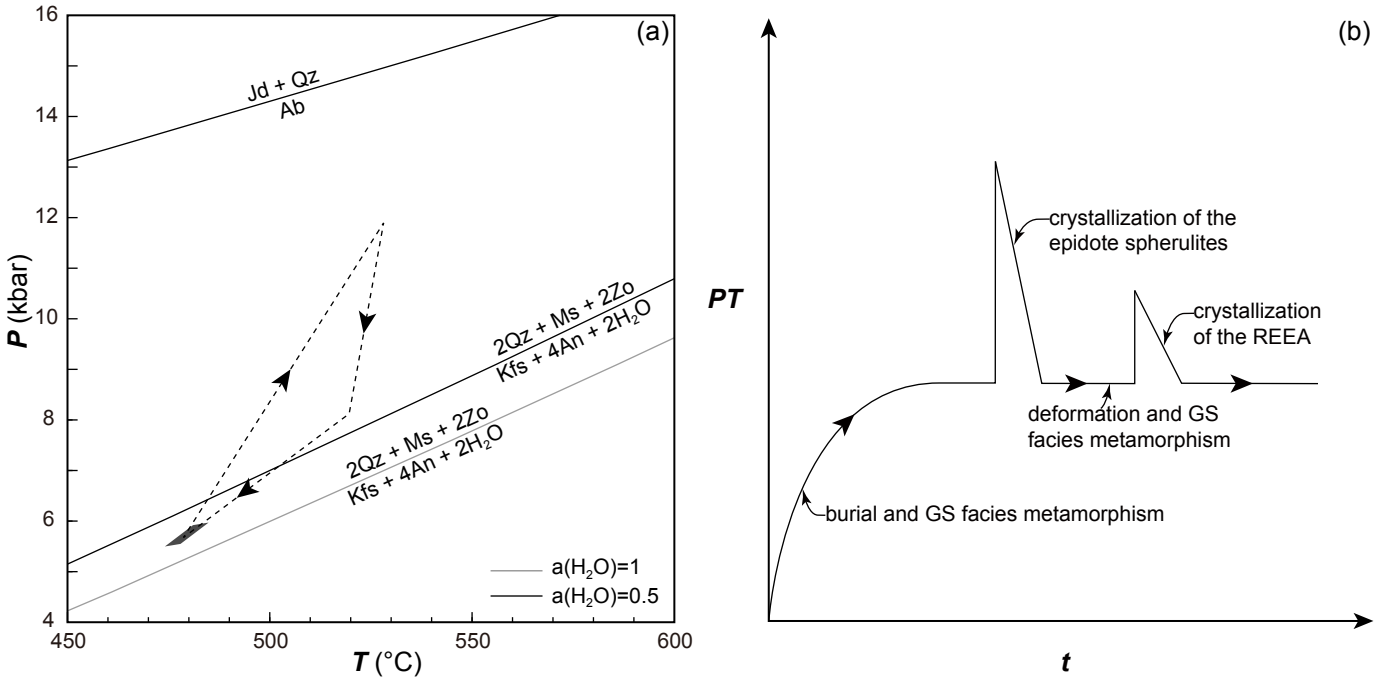

This is a preprint, the final version is subject to change, of the American Mineralogist (MSA)
Cite as Authors (Year) Title. American Mineralogist, in press.
DOI: https://doi.org/10.2138/am-2019-6980

Table 1 Representative epidote compositions in the epidote spherulites and radial euhedral epidote aggregates (REEA)

texture	fibrous							inclusion		interfibrilliar		euhedral overgrowth			in REEA (	
number	1	2	3	4	5	6	7	8	9	10	11	13	14	15	16	17
SiO_2	36.11	36.37	35.99	37.22	36.70	35.89	36.54	37.49	37.31	37.10	37.64	37.45	37.22	37.99	37.56	38.04
TiO_2	0.08	0.06	0.11	0.05	0.11	0.07	0.06	0.02	0.04	0.06	0.06	0.04	0.08	0.06	0.16	0.06
Al_2O_3	21.59	21.81	21.26	23.76	22.54	21.63	22.81	22.49	23.06	23.08	23.15	22.73	23.27	24.34	23.67	23.30
FeO	12.30	11.94	12.34	12.05	12.13	12.62	12.24	12.58	12.24	12.09	12.10	12.81	12.17	11.35	11.78	12.24
MnO	0.75	0.74	0.59	0.61	0.49	0.60	0.60	0.95	0.48	0.51	0.54	0.83	0.60	0.12	1.00	0.74
MgO	0.28	0.25	0.27	0.12	0.18	0.21	0.17	0.11	0.11	0.08	0.10	0.03	0.08	0.05	0.05	0.06
CaO	19.28	19.39	17.87	20.40	20.09	19.62	20.20	21.48	21.31	21.74	22.19	22.87	22.31	23.62	23.06	22.89
Na_2O	0.04	0.00	0.08	0.05	0.00	0.01	0.05	0.00	0.00	0.00	0.02	0.02	0.05	0.01	0.02	0.01
K_2O	0.00	0.00	0.00	0.00	0.00	0.01	0.00	0.02	0.00	0.00	0.00	0.05	0.01	0.00	0.01	0.00
La_2O_3	3.82	3.01	3.22	1.21	1.64	3.19	1.62	0.92	1.03	0.68	0.81	0.10	0.65	0.08	0.00	0.43
Ce_2O_3	3.38	2.89	5.32	1.81	2.81	3.23	2.76	1.33	1.84	1.34	1.30	0.48	0.74	0.06	0.00	0.42
Pr_2O_3	0.00	0.00	0.03	0.00	0.03	0.00	0.00	0.00	0.00	0.00	0.05	0.00	0.00	0.00	0.00	0.00
Nd_2O_3	0.23	0.27	1.12	0.54	0.67	0.45	0.51	0.03	0.29	0.14	0.05	0.03	0.08	0.07	0.00	0.13
Sm_2O_3	0.00	0.00	0.00	0.02	0.35	0.00	0.00	0.00	0.06	0.06	0.00	0.00	0.07	0.00	0.00	0.32
Eu_2O_3	0.11	0.20	0.07	0.30	0.09	0.00	0.18	0.30	0.10	0.20	0.25	0.20	0.01	0.00	0.00	0.07
Gd_2O_3	0.00	0.18	0.05	0.13	0.14	0.00	0.00	0.00	0.05	0.00	0.00	0.00	0.00	0.00	0.00	0.00
Y_2O_3	0.00	0.00	0.00	0.28	0.08	0.12	0.06	0.02	0.13	0.15	0.01	0.07	0.13	0.04	0.02	0.10
Total	97.97	97.12	98.32	98.54	98.04	97.64	97.80	97.74	98.02	97.22	98.26	97.69	97.48	97.79	97.32	98.80
O=12.5																
Si	3.00	3.02	3.02	2.99	3.00	2.98	2.98	3.01	3.00	2.99	3.00	2.98	2.97	2.99	2.97	3.00
Ti	0.00	0.00	0.01	0.00	0.01	0.00	0.00	0.00	0.00	0.00	0.00	0.00	0.00	0.00	0.01	0.00
Al	2.11	2.14	2.10	2.25	2.17	2.11	2.19	2.13	2.19	2.19	2.17	2.13	2.19	2.25	2.21	2.16
Fe^{3+}	0.67	0.61	0.55	0.64	0.64	0.71	0.69	0.76	0.70	0.74	0.75	0.85	0.81	0.75	0.78	0.80
Fe^{2+}	0.19	0.22	0.32	0.17	0.19	0.17	0.14	0.08	0.12	0.07	0.05	0.00	0.00	0.00	0.00	0.01
Mn	0.05	0.05	0.04	0.04	0.03	0.04	0.04	0.06	0.03	0.03	0.04	0.06	0.04	0.01	0.07	0.05
Mg	0.03	0.03	0.03	0.01	0.02	0.03	0.02	0.01	0.01	0.01	0.01	0.00	0.01	0.01	0.01	0.01
Ca	1.71	1.73	1.61	1.76	1.76	1.74	1.76	1.85	1.84	1.88	1.89	1.95	1.91	1.99	1.95	1.93
Na	0.01	0.00	0.01	0.01	0.00	0.00	0.01	0.00	0.00	0.00	0.00	0.00	0.01	0.00	0.00	0.00
K	0.00	0.00	0.00	0.00	0.00	0.00	0.00	0.00	0.00	0.00	0.00	0.00	0.00	0.00	0.00	0.00
La	0.12	0.09	0.10	0.04	0.05	0.10	0.05	0.03	0.03	0.02	0.02	0.00	0.02	0.00	0.00	0.01
Ce	0.10	0.09	0.16	0.05	0.08	0.10	0.08	0.04	0.05	0.04	0.04	0.01	0.02	0.00	0.00	0.01
Pr	0.00	0.00	0.00	0.00	0.00	0.00	0.00	0.00	0.00	0.00	0.00	0.00	0.00	0.00	0.00	0.00
Nd	0.01	0.01	0.03	0.02	0.02	0.01	0.01	0.00	0.01	0.00	0.00	0.00	0.00	0.00	0.00	0.00
Sm	0.00	0.00	0.00	0.00	0.01	0.00	0.00	0.00	0.00	0.00	0.00	0.00	0.00	0.00	0.00	0.01
Eu	0.00	0.01	0.00	0.01	0.00	0.00	0.00	0.01	0.00	0.01	0.01	0.01	0.00	0.00	0.00	0.00
Gd	0.00	0.00	0.00	0.00	0.00	0.00	0.00	0.00	0.00	0.00	0.00	0.00	0.00	0.00	0.00	0.00
Y	0.00	0.00	0.00	0.01	0.00	0.01	0.00	0.00	0.01	0.01	0.00	0.00	0.01	0.00	0.00	0.00
Sum	8.00	8.00	8.00	8.00	8.00	8.00	8.00	8.00	8.00	8.00	8.00	8.00	8.00	8.00	8.00	8.00
REE_{tol}	0.23	0.20	0.30	0.13	0.17	0.21	0.15	0.08	0.10	0.08	0.07	0.03	0.05	0.01	0.00	0.04
$Fe^{2+}+Fe^{3+}+Al^{3+}+Mg$	3.00	3.00	3.01	3.07	3.02	3.02	3.05	2.99	3.02	3.02	2.99	2.98	3.01	3.01	2.99	2.98
$Mn^{2+}+Ca+REE_{tol}$	2.00	1.98	1.95	1.93	1.97	2.00	1.96	1.99	1.97	1.99	2.00	2.03	2.00	2.00	2.02	2.02
Fe_2O_3	10.67	9.81	8.63	10.65	10.37	11.34	11.29	12.58	11.59	12.24	12.55	14.24	13.47	12.61	13.09	13.46
FeO	2.70	3.12	4.58	2.46	2.80	2.42	2.08	1.26	1.81	1.07	0.80	0.00	0.05	0.00	0.00	0.13

Note: "-" denotes not analyzed. REEA=radial euhedral epidote aggregates.

REE-poor)		in REEA (REE-zoned)				individual euhedral			
18	**19**	**21**	**22**	**23**	**24**	**26**	**27**	**28**	**29**
38.33	38.08	37.30	37.93	38.20	34.59	37.69	37.57	37.61	38.06
0.07	0.12	0.05	0.12	0.06	0.11	0.07	0.06	0.03	0.11
23.39	24.24	23.74	23.81	24.32	19.95	23.60	24.52	23.06	23.24
12.64	11.71	11.01	11.27	11.63	11.84	12.54	11.61	12.98	12.91
0.77	0.87	1.50	1.13	0.43	1.52	0.88	0.98	0.64	0.63
0.00	0.05	0.05	0.03	0.03	0.57	0.01	0.02	0.01	0.02
23.04	22.83	20.63	21.96	22.39	14.74	22.15	22.40	22.69	22.75
0.00	0.00	0.02	0.04	0.01	0.06	0.02	0.00	0.00	0.01
0.02	0.02	0.01	0.03	0.02	0.03	0.03	0.01	0.05	0.02
0.10	0.04	0.66	0.23	0.00	1.87	-	-	-	-
0.11	0.03	1.43	0.17	0.02	7.37	-	-	-	-
0.00	0.00	0.00	0.00	0.07	0.00	-	-	-	-
0.00	0.00	0.48	0.06	0.00	3.87	-	-	-	-
0.00	0.05	0.15	0.00	0.00	0.28	-	-	-	-
0.17	0.00	0.33	0.02	0.10	0.03	-	-	-	-
0.00	0.00	0.00	0.00	0.00	0.11	-	-	-	-
0.01	0.02	0.08	0.10	0.01	0.29	-	-	-	-
98.64	98.05	97.43	96.90	97.31	97.22	96.99	97.18	97.07	97.75
3.01	2.99	3.01	3.02	3.02	3.03	3.00	2.97	2.99	3.01
0.00	0.01	0.00	0.01	0.00	0.01	0.00	0.00	0.00	0.01
2.16	2.24	2.26	2.24	2.27	2.06	2.21	2.29	2.16	2.16
0.81	0.76	0.63	0.69	0.68	0.43	0.79	0.76	0.86	0.82
0.02	0.01	0.11	0.06	0.09	0.44	0.04	0.01	0.00	0.04
0.05	0.06	0.10	0.08	0.03	0.11	0.06	0.07	0.04	0.04
0.00	0.01	0.01	0.00	0.00	0.07	0.00	0.00	0.00	0.00
1.94	1.92	1.78	1.88	1.90	1.38	1.89	1.90	1.93	1.92
0.00	0.00	0.00	0.01	0.00	0.01	0.00	0.00	0.00	0.00
0.00	0.00	0.00	0.00	0.00	0.00	0.00	0.00	0.00	0.00
0.00	0.00	0.02	0.01	0.00	0.06	-	-	-	-
0.00	0.00	0.04	0.00	0.00	0.24	-	-	-	-
0.00	0.00	0.00	0.00	0.00	0.00	-	-	-	-
0.00	0.00	0.01	0.00	0.00	0.12	-	-	-	-
0.00	0.00	0.00	0.00	0.00	0.01	-	-	-	-
0.00	0.00	0.01	0.00	0.00	0.00	-	-	-	-
0.00	0.00	0.00	0.00	0.00	0.00	-	-	-	-
0.00	0.00	0.00	0.00	0.00	0.01	-	-	-	-
8.00	8.00	8.00	8.00	8.00	8.00	8.00	8.00	8.00	8.00
0.01	0.00	0.09	0.02	0.01	0.44	-	-	-	-
2.99	3.02	3.01	2.99	3.04	3.00	3.05	3.06	3.03	3.02
2.00	1.98	1.98	1.97	1.93	1.94	1.95	1.96	1.98	1.97
13.73	12.85	10.38	11.54	11.45	6.47	13.24	12.82	14.35	13.75
0.28	0.15	1.68	0.88	1.32	6.01	0.63	0.08	0.07	0.54

This is a preprint, the final version is subject to change, of the American Mineralogist (MSA)
Cite as Authors (Year) Title. American Mineralogist, in press.
DOI: https://doi.org/10.2138/am-2019-6980

Table 2 Representative electron microprobe analyses of minerals in the matrix

	Plagioclase	K-feldspar	Phengite	Biotite	epidote	Garnet	Hematite
SiO_2	65.24	63.84	46.53	37.40	38.47	37.25	0.31
TiO_2	0.07	0.07	0.91	2.00	0.13	0.15	0.01
Al_2O_3	21.60	18.50	28.80	15.15	24.32	20.32	0.13
Cr_2O_3	0.00	0.00	0.00	0.00	0.00	0.01	0.08
FeO	0.22	0.08	6.41	19.75	11.66	16.16	90.91
MnO	0.00	0.00	0.05	0.85	0.07	15.44	0.00
MgO	0.00	0.02	1.98	10.36	0.06	0.88	0.00
CaO	2.49	0.04	0.02	0.35	22.19	9.23	0.01
Na_2O	10.31	0.48	0.26	0.08	0.01	0.00	0.01
K_2O	0.16	15.62	10.59	9.36	0.00	0.00	0.00
Total	100.10	98.66	95.55	95.30	96.91	99.45	91.46
Si	2.86	2.98	3.18	2.86	3.03	3.00	0.01
Ti	0.00	0.00	0.05	0.11	0.01	0.01	0.00
Al	1.15	1.03	2.32	1.37	2.28	1.93	0.00
Cr	0.00	0.00	0.00	0.00	0.00	0.00	0.00
Fe^{2+}	0.01	0.00	0.37	1.26	0.13	1.06	0.00
Mn	0.00	0.00	0.00	0.06	0.00	1.05	0.00
Mg	0.00	0.00	0.20	1.18	0.01	0.11	0.00
Ca	0.12	0.00	0.00	0.03	1.89	0.80	0.00
Na	0.87	0.05	0.03	0.01	0.00	0.00	0.00
K	0.01	0.92	0.92	0.91	0.00	0.00	0.00
Fe^{3+}	-	-	-	-	0.65	0.04	1.98
Total	5.01	4.99	7.09	7.80	8.00	8.00	2.00

This is a preprint, the final version is subject to change, of the American Mineralogist (MSA)
Cite as Authors (Year) Title. American Mineralogist, in press.
DOI: https://doi.org/10.2138/am-2019-6980

Table 3 Representative electron microprobe analyses of minerals in the plagioclase pseudomorphs

	Plagioclase					K-feldspar			Phengite					Epidote
SiO_2	65.47	65.39	66.67	65.84	65.44	63.69	63.50		46.28	46.43	46.00	46.93	46.01	38.40
TiO_2	0.00	0.00	0.01	0.00	0.00	0.02	0.01		0.44	0.35	0.40	0.39	0.37	0.13
Al_2O_3	21.88	21.73	20.79	22.07	22.18	19.16	19.62		28.72	28.58	28.78	28.64	28.86	25.35
Cr_2O_3	0.01	0.00	0.00	0.00	0.00	0.01	0.00		0.00	0.01	0.00	0.00	0.01	0.02
FeO	0.24	0.13	0.14	0.16	0.14	0.03	0.02		6.43	6.52	6.60	6.04	6.30	9.30
MnO	0.03	0.03	0.02	0.00	0.00	0.00	0.00		0.06	0.06	0.07	0.05	0.10	0.79
MgO	0.03	0.00	0.01	0.01	0.00	0.00	0.00		2.00	1.96	1.91	1.95	2.00	0.08
CaO	1.97	1.85	1.03	2.09	2.15	0.01	0.00		0.04	0.05	0.03	0.05	0.03	22.26
Na_2O	10.37	10.37	10.94	10.32	10.30	0.27	0.39		0.27	0.27	0.25	0.29	0.27	0.14
K_2O	0.25	0.13	0.20	0.18	0.13	15.75	15.65		10.67	10.74	10.67	10.64	10.63	0.26
Total	100.24	99.64	99.82	100.69	100.33	98.94	99.19		94.93	94.98	94.74	94.98	94.58	96.74
Si	2.87	2.88	2.90	2.87	2.87	2.97	2.95		3.19	3.20	3.18	3.22	3.18	3.03
Ti	0.00	0.00	0.00	0.00	0.00	0.00	0.00		0.02	0.02	0.02	0.02	0.02	0.01
Al	1.13	1.13	1.10	1.14	1.15	1.05	1.08		2.33	2.32	2.35	2.32	2.35	2.36
Cr	0.00	0.00	0.00	0.00	0.00	0.00	0.00		0.00	0.00	0.00	0.00	0.00	0.00
Fe^{2+}	0.01	0.00	0.01	0.01	0.01	0.00	0.00		0.37	0.38	0.38	0.35	0.36	0.00
Mn	0.00	0.00	0.00	0.00	0.00	0.00	0.00		0.00	0.00	0.00	0.00	0.01	0.05
Mg	0.00	0.00	0.00	0.00	0.00	0.00	0.00		0.21	0.20	0.20	0.20	0.21	0.01
Ca	0.09	0.09	0.09	0.10	0.10	0.00	0.00		0.00	0.00	0.00	0.00	0.00	1.88
Na	0.88	0.89	0.90	0.87	0.88	0.02	0.03		0.04	0.04	0.03	0.04	0.04	0.02
K	0.01	0.01	0.01	0.01	0.01	0.94	0.93		0.94	0.95	0.94	0.93	0.94	0.03
Fe^{3+}	-	-	-	-	-	-	-		-	-	-	-	-	0.61
Total	5.01	5.00	5.01	5.00	5.00	4.98	4.99		7.11	7.11	7.11	7.08	7.11	8.00
X_{An}	0.09	0.09	0.09	0.10	0.10	0.00	0.00	X_{Pg}	0.037	0.037	0.035	0.039	0.038	
X_{Ab}	0.89	0.90	0.90	0.89	0.89	0.03	0.04	Fe/Mg	1.80	1.86	1.94	1.74	1.77	
X_{Kfs}	0.01	0.01	0.01	0.01	0.01	0.97	0.96							